Superior multifunctional activity of nanoporous carbons with widely tuneable porosity: enhanced storage capacities for carbon-dioxide, hydrogen, water and electric charge

Srinivas Gadipelli, Christopher A. Howard, Jian Guo, Neal T. Skipper, Hong Zhang, Paul R. Shearing, and Dan J. L. Brett*

Dr. S. Gadipelli, Prof. H. Zhang
College of Physics, Sichuan University, Chengdu 610064, China
E-mail: s.gadipelli@ucl.ac.uk

Dr. S. Gadipelli, Prof. P. R. Shearing, Prof. D. J. L. Brett
Electrochemical Innovation Lab, Department of Chemical Engineering, University College London, London WC1E 7JE, United Kingdom

Dr. C. A. Howard, Prof. N. T. Skipper
Department of Physics & Astronomy, University College London, London WC1E 6BT, United Kingdom

J. Guo
Department of Chemistry, University College London, London WC1H 0AJ, United Kingdom

Prof. P. R. Shearing, Prof. D. J. L. Brett
The Faraday Institution, Quad One, Harwell Science and Innovation Campus, OX11 0RA, Didcot, UK

Keywords: nanoporous carbon and multifunctional activity; carbon-based electric-double layer capacitors (EDLCs); carbon-dioxide capture; water capture; hydrogen storage; high energy supercapacitors

Abstract

Nanoporous carbons (NPCs) with engineered specific pore-sizes and sufficiently high porosities (both specific surface area and pore volume) are necessary for storing energy in the form of electric charges and molecules. Herein, NPCs, derived from biomass pine-cones, coffee-grounds, graphene-oxide and metal-organic frameworks, with systematically increased pore-widths (<1.0 nm to few nm), micropore-volume (0.2-0.9 $cm^3\ g^{-1}$) and specific surface area (800-2800 $m^2\ g^{-1}$) are presented. Superior CO_2, H_2 and H_2O uptakes of 35.0 wt% (≈7.9 mmol g^{-1} at 273 K), 3.0 wt% (at 77 K) and 85.0 wt% (at 298 K), respectively at 1 bar, are achieved. At controlled microporosity, supercapacitors deliver impressive performance with a capacity of 320 and 230 F g^{-1} at 500 mA g^{-1}, in aqueous and organic electrolytes,

respectively. Excellent areal capacitance and energy density (>50 Wh kg^{-1} at high power density 1000 W kg^{-1}) are achieved to form the highest reported values among the range of carbons in the literature. The noteworthy energy storage performance of the NPCs for all five cases (CO_2, H_2, H_2O and capacitance in aqueous and organic electrolytes) is highlighted by direct comparison to numerous existing porous solids. A further analysis on the specific pore type governed physisorption capacities is presented.

Introduction

Nanoporous carbons (NPCs) are promising for many guest molecular sorption, storage and separation/distribution applications due to their flexible chemical nature, high thermal, mechanical and chemical stability, and electrical conductivity.[1-6] In most cases, the specific application of the porous carbons is directly determined by their accessible porosity parameters: specific surface area (SSA_{BET}), pore-size distribution and pore volume. The sp^2 components of the open carbon skeletons are beneficial in many electrochemical energy conversion and storage applications, such as electrocatalysts in fuel-cells and metal-air batteries, and charge storage and distribution in supercapacitors. Supercapacitors, in particular, carbon-based electric double-layer capacitor (EDLC), require porous carbons with engineered pore widths for the targeted electrolyte charge storage. These fascinating and versatile characteristics make carbons of special interest compared to other porous solids such as zeolites, metal-organic frameworks (MOFs) or coordinated/cross-linked polymers (CPs), and other layered materials. Therefore, these materials are being actively and continuously explored and numerous synthesis routes are proposed.[1-31] For example, the templates of pre-synthesised molecular architectures of mesoporous silica, CPs, MOFs and zeolites are often used to achieve control over porosities. In both top-down and bottom-up approaches, the carbons can be derived from carbides (known as CDCs), graphites (or graphene-oxide, GO),

and carbonised biomass or renewables, polymers (or its coordinated complexes) and MOFs, as well as molecular CVD routes.

Such materials exhibit a wide range of porosities, with ultra-high surface area being particularly targeted.[4-17,20,21,23-38,40-44,48-59] These high porosities are achieved by simultaneously increasing the pore-widths across several nanometres – commonly defined to be: microporosity, mesoporosity and macroporosity respectively for pore-widths of ≤2 nm, (2-50) nm and ≥50 nm. Ultra-porosity or high surface area in carbons is always associated with the further increase in pore-sizes and their distribution, due to the continual etching of already formed micropores and/or with a high concentration of salt melts as porogenes or with the template structures. All these design efforts are exclusively directed towards high capacity guest adsorption for storing gas and liquid/vapour molecules, and electric charges. Although the specific surface area is an important parameter to determine the adsorptive capacities, the pore-widths, pore-size distribution and surface heterogeneity (with heteroatom dopants) all play a further major role in attaining desirable storage characteristics, such as to enable extensive accumulation, distribution, binding, diffusion and kinetics. It is also worth pointing out that the high porosity in the materials necessarily reduces the density of the interconnected networks of carbons and also introduces high defective carbon content in the structure to be more electrically resistive. Thus, for example, carbons often exhibit poor areal and volumetric EDLC capacities contrary to the requirements for smart electronics applications. While historical guidelines exist in the literature to optimise the sorbent structure for maximising their guest storage capacity, the recent past literature (selected to be exclusively from between the years 2018 and 2019) shows widely distributed capacities with significant inconsistencies (see tabulated capacities against SSA_{BET} of the materials, for example large amount of data deduced for CO_2 and EDLC, in **Tables S1 to S3** in

Supplementary Information).[4,5,7,15,23,29,31-35,42-44,49-55] In numerous cases, targeted structures perform worse than anticipated, and often exhibit considerably varied adsorptive capacities.

Herein, the development of NPCs with extended range porosities is reported by utilising biomass pine-cones and coffee-grounds, and GO and MOFs precursor materials (the resultant carbon products are named as PMCs, CMCs, GCs and MCs, respectively). The synthesis conditions including precursor types have a profound effect on the porosity development and pore-size distribution in the final products. The mild synthesis conditions of pine-cones yield ultramicroporous carbons (UMCs), with a pore-size distribution strictly below 1.5 nm scale, and (91-97)% of total porosity at less than 1.0 nm pore-widths. The UMCs also exhibit a high SSA_{BET} of ≈1600 $m^2\ g^{-1}$ and porosity of ≈0.6 $cm^3\ g^{-1}$. Later, the synthesis is modified to controllably increase the porosity to a large extent to reach a surface area of 2800 $m^2\ g^{-1}$ and micropore volume of 1.00 $cm^3\ g^{-1}$ with systematically increased pore-widths across microporous to mesoporous region. Such porosity characteristics result in high molecular uptake capacities at low-pressures (≤1 bar), for example, adsorbing up to 7.9 mmol g^{-1} (≈34.6 wt%) of CO_2 at 273 K and ≈3.0 wt% of H_2 at 77 K. The samples also exhibit high water vapour uptake, reaching 85 wt% at 298 K. Moreover, symmetric supercapacitors show impressive specific gravimetric capacitance of 320 and 230 F g^{-1} at 500 mA g^{-1} and rate capacitance, in aqueous (6 M KOH) and organic (a nonaqueous, 1 M $TEABF_4$/AC – tetraethylammonium tetrafluoroborate in acetonitrile) electrolytes, respectively. The UMCs with specific porosity yield an exceptional areal capacitance, 20-16 µF cm^{-2}, far higher than ≤10 µF cm^{-2} reported for the very high porosity carbons in the literature. Similarly, at a controlled microporosity, the organic and aqueous supercapacitors deliver excellent energy density of ≈51 and 7.0 Wh kg^{-1}, respectively, at a high power density of ≈1000 W kg^{-1}. Thus the storage capacities in our controlled-porosity NPCs, are forming the top values (8.0 mmol

g^{-1} of CO_2, 3.0 wt% of H_2, 85.0 wt% H_2O and 320 F g^{-1} or 230 F g^{-1} of EDLC in aqueous or organic electrolyte, with areal capacitance of 20 µF cm^{-2} and energy density >50 Wh kg^{-1}) among the numerous related materials reported in the literature and also for a range of multifunctional applications. The comparative analysis demonstrates that the NPCs of specific pore-widths exhibit the highest storage capacities at SSA_{BET} range of 2000-2500 m^2 g^{-1} for all five case applications reported in this study. Further increase in surface area results in considerable pore-size widening and does not further promote uptake capacities. The specific pore size (in the region of ultramicroporosity to microporosity and mesoporosity) and pore type (such as slit, cylindrical and spherical) guided physisorption capacities is schematically presented and discussed.

Results and discussion

As shown in **Figure 1** and Figure S1 in Supplementary Information, and described in Experimental details, the NPCs are produced from different precursor materials under controlled synthesis conditions. The starting materials used are the abundant biomass, pine-cones and coffee-grounds, and GO and MOFs (MOF-5). To begin with, the UMCs samples are produced by, firstly, biomass condensation to chars at mild thermolysis temperatures between 250 and 550 °C, followed by KOH (potassium hydroxide)-based chemical activation at 750 °C. Thermogravimetry on dried pine-cones reveals interesting information on carbonisation behaviour (**Figure 1a**). Initially, mass is lost at ≥200 °C due to the evaporation of volatile oxygen complexes. Comparatively less mass-loss between 350 and 550 °C indicates the condensation/carbonisation region - a transformation of biomass to biochar (BC). Therefore, a range of different temperatures between 250 and 550 °C are selected for pre-treating the pine cones before subjecting them for chemical activation. The degree of carbonisation (graphitisation) can be seen in their respective Raman spectra (**Figure 1b**). The

BC250 sample exhibits no Raman active carbon modes; however, the carbonisation induced C–C aromatic stretching mode, G-band, appears in sample BC350. A more prominent Raman G-band is observed in BC550. Here it is worth noting that the pine-cones and biochar samples are non-porous in nature (Figure S2 in Supplementary Information). Therefore, in order to produce porous carbons, and also to understand the significance of the carbonisation transformation, the chars are blended with aqueous KOH at a constant mass ratio of 1:3 of BC to KOH and activated at 750 °C. Final products are named as UMC250, UMC350, UMC450 and UMC550, with respect to the temperature of the chars.

Structural characteristics of the activated products reveal distinctly different nature compared to the precursor chars. A considerable broadening of the G-band together with a prominent D-band in the Raman spectra indicates a high percentage of defective or edge sp^3 carbon in the sp^2 skeleton (**Figure 1c**). Furthermore, the loss of structural order in the Raman modes at 2800-3200 cm^{-1} and weak graphitic order at 2θ of ≈25° (out of plane) or ≈44° (in-plane) diffraction peaks in powder X-ray diffraction (PXRD) signifies the amorphous and turbostratic nature of small graphitic fragments (**Figure 1d,** Figure S3 in Supplementary Information). X-ray photoemission spectra (XPS) show up to 88 atom% of carbon, with remaining oxygen only as heteroatoms (**Figure 1e,** Figure S4 in Supplementary Information). Deconvolution of core level C 1s spectra shows the defective sp^3 C, in the form of C–O and O–C=O at ≈285.3 eV and ≈288.5 eV, with the remaining graphitic sp^2 C, C=C at ≈284.6 eV (**Figure 1f,** and Figure S4, Table S4 in Supplementary Information). This is further evidenced at core level spectra of O 1s, with C–OH (at ≈532.6 eV) and C=O (at ≈531.4 eV).[24,25] Scanning and transmission electron micrographs (SEM and TEM) reveal the surface morphology of the samples (**Figure 1g,h,** Figure S5 in Supplementary Information). The development of porosity is clearly visible relative to the precursor char. TEM micrographs

show a highly microporous carbon type, as the samples are produced under mild and controlled synthesis conditions. SEM images reveal flake type morphology with carbon particle size distribution below 10 microns.

More quantitative measurements of the porosity are obtained by nitrogen and carbon-dioxide adsorption-desorption isotherms with Brunauer-Emmett-Teller (BET) and density functional theory (DFT) analysis (**Figure 2a,b, Table 1,** Figure S6 in Supplementary Information, and Experimental details). All the isotherms represent Type-I microporous nature and yield SSA_{BET} of 1130, 1420, 1620, and 826 $m^2\ g^{-1}$ and pore volume of 0.461, 0.567, 0.658, and 0.323 $cm^3\ g^{-1}$, respectively for UMC250, UMC350, UMC450, and UMC550. Specifically, the samples are ultra-microporous with the pore-size distribution (PSD) strictly limited to less than 1.5 nm, and mostly developed at ≤1.0 nm (**Figure 2b**). Such characteristics account for (91-97)% of total porosity, situated at below 1.0 nm sized pore-widths (**Table 1**). Note that the QSDFT-deduced cumulative pore volume is in good agreement with the pore volume obtained by the measured N_2 adsorption isotherm data. The samples also show a well-correlated linear relationship between the SSA_{BET} and pore volume, estimated at various pore-widths of 1.0 nm, 2.0 nm and total pore volume (**Figure 2c**). The optimised synthesis conditions yield control over pore-widths and distribution.

The porosity characteristics in the UMCs are further evidenced by their high adsorption capacities for carbon dioxide, hydrogen and water (**Figure 2d to 2i, Table 1** and Table S3 in Supplementary Information). CO_2 uptake isotherms measured at 273 K show a clear porosity-dependent uptake trend (**Figure 2d,g**). Specifically, at a low CO_2 partial pressure of 0.15 bar, as a standard concentration in the post-combustion flue-gas, the samples with ultra-narrow pores show high CO_2 capture capacity, reaching to 2.75 mmol g^{-1} (≈12.1 wt%). The

maximum capacity of 7.9 mmol g^{-1} (≈34.6 wt%) at 1 bar is also one of the highest values reported so far in the wide range of porous solids, including N-doped activated carbons (ACs), MOFs (of open-metal centres, micropores and flexible frameworks), microporous polymers, and solid-amines.[5,6,10,14,23-25,27-41] Uptake values deduced at 273 K and 1 bar in such different categories of materials family with respect to their SSA_{BET} are comparatively summarised in **Figure 2g**. Interestingly, CO_2 uptakes in high SSA_{BET} samples appear to show comparable or even lower capacities than UMCs. More importantly, the recent reviews reportedly show that the biomass-derived porous carbons yield maximum CO_2 uptake of about 7.0-7.7 mmol g^{-1} at the surface area of 1535-2110 m^2 g^{-1}.[3,5] Also here it is worth mentioning that in many of the recent literature (from 2018), numerous higher surface area carbon samples derived from a wide range of precursors show reduced uptakes (**Figure 2g,** Table S3 in Supplementary Information**)**. Some of the existing ultra-microporous solids belonging to the CDCs, open-metal MOFs, and biomass or natural renewables derived carbons and multiple heteroatom doped carbons with the SSA_{BET} <1800 m^2 g^{-1} are found to exhibit somewhat similar capacities.[27,28,36] The samples appear to show maximum CO_2 uptakes when their pore-sizes are controlled within the 1.0 nm. For instance, the sample that exhibits predominant porosity of around 0.7 nm along with a much smaller proportion of pores of size below 1.5 nm and SSA_{BET} of 1551 m^2 g^{-1} has shown CO_2 uptake of 7.4 mmol g^{-1}.[36] Microporous carbons derived from coffee-waste show CO_2 capacity of 7.5 and 7.2 mmol g^{-1} for SSA_{BET} of 1620 and 2070 m^2 g^{-1}, respectively with more than 90% of the porosity is in the <1.5 nm region.[40] UMCs also exhibit a clear porosity-dependent uptake trend, where a linear correlation can be established between uptakes and SSA_{BET} or micropore volume (**Figure 2c,g**). The high CO_2 capacities in the UMCs are further well supported by the H_2 and water vapour uptake uptakes, which exhibit impressive capacities when compared to the similar surface area porous solids (**Figure 2e,f,h,i**). For instance, due to their ultra-

microporosity, a significant amount of water adsorption (>25 wt%) is observed at relatively low humidity levels of under 35% relative humidity, RH (Figure S7 in Supplementary Information). Note that UMC250 and UMC350 samples show enhanced uptakes and kinetics compared to the high porosity UMC450 sample that has a slightly larger pore size distribution.

Next, the electrochemical energy storage performance of the UMCs is investigated by constructing two-electrode symmetric supercapacitors with aqueous (6 M KOH) electrolyte (Experimental details). The characteristic cyclic voltammetry (CV) curves and galvanostatic charge-discharge (GCD) curves represent EDLC behaviour (**Figure 3a to 3d,** Figure S8 in Supplementary Information). GCD curves at different applied current densities between 100 mA g^{-1} and 25 A g^{-1} indicates the large specific capacitance values, reaching 310 F g^{-1} at 100 mA g^{-1}, and 273 and 260 F g^{-1} at 0.5 and 1.0 A g^{-1} (**Figure 3e, Table 1** and Figures S8 in Supplementary Information). UMC350, with its lower porosity, shows enhanced capacitance. The UMCs show good cyclic stability with retention of initial capacitance value >220 F g^{-1} at 5.0 A g^{-1} when tested for 4000 cycles (**Figure 3f**). Interestingly, all the adsorptive capacities, EDLC, CO_2, H_2 and H_2O uptakes, data vary in a similar manner, linearly with respect to the SSA_{BET} or pore volume (**Figures 2 and 3g**). Here it is interesting to note that with respect to the SSA_{BET} the UMCs show relatively high gravimetric as well as areal (surface area normalised capacitance, C_{SSA}) EDLC capacity when compared to numerous other high surface area carbons in the literature (**Figure 3g,h,i**).[7,9,11,13,15-23,26,34,49-59] The EDLC capacities (deduced at current loads of 0.5-1.0 A g^{-1}) of the high surface area carbons from literature are summarily presented in **Figure 3g** (**Table 1** and Table S1 in Supplementary Information). As per comparative data represented in **Figure 3i**, the UMC450 (with SSA_{BET} of 1620 m^2 g^{-1}) exhibits equally good rate performance. Here it is worth

mentioning that even though ultramicroporous carbons have been reported in the literature their porosities and capacities are not superior to our UMCs.[3,5,6,18,19,22,23,25-41] For instance, those ultra-microporous carbons, prepared under KOH activation, with nitrogen doping show CO_2 and EDLC values of 6.0-7.2 mmol g^{-1} and 140-310 F g^{-1}, which are lower than the capacities observed in our UMCs (**Table 1,** and Table S3 in Supplementary Information).[19,22,29,37] The literature samples also exhibit relatively lower porosities (SSA_{BET} of 600-1500 m^2 g^{-1} and pore volume of 0.3-0.54 cm^3 g^{-1}). Moreover these materials do not demonstrate any correlation for the CO_2 uptakes with the N-doping.[28,29,31,36,37-39] In another case, microporous carbons yield limited porosities with SSA_{BET} of 700-1312 m^2 g^{-1}.[18] These samples also show considerably lower capacities for both the cases – for example the capacitance of only 200 F g^{-1} at 0.5 A g^{-1} and CO_2 uptake of <6.77 mmol g^{-1} are much lower than our UMCs.

Building on the impressive energy storage performance of UMCs, and for further advancements in capacities and insights, several further families of high porosity NPCs (PMCs, CMCs, GCs, and MCs) are synthesized with extended surface areas and pore volumes at systematically increased pore-widths and their distribution across the microporous/ mesoporous region (**Figure 4, Table 1,** and Experimental details and structural characteristics in Supplementary Information). As shown in **Figure 4a**, the pore-widths in PMCs and CMCs (microporous carbons of pine-cones and coffee-grounds) can be gradually increased in a controlled fashion. These samples are predominantly microporous in nature (**Figures 4a,b,c**). The N_2 isotherms are in Type-I with the gradually increased knee slope at low relative pressures, 0-0.1, indicating the broadening of pore size and pore size distribution with an increase in surface area and total pore volume. The samples show relatively high surface areas as well as pore volumes than UMCs between 1800-2600 m^2 g^{-1} and 0.70-1.13

$cm^3\ g^{-1}$ (**Table 1**). It is interesting to note that the ultramicroporosity at 1.0 nm pore-widths is enhanced over UMCs to 0.64 $cm^3\ g^{-1}$ at SSA_{BET} of 2200 $m^2\ g^{-1}$, where further increase in SSA_{BET} is shown to develop the larger pores in the near mesoporous region. **Figure 4c** shows no further increase in the micropore volume at pore sizes of 1.0 or 2.0 nm when SSA_{BET} is increased beyond 2000 or 2500 $m^2\ g^{-1}$, respectively. Here, a proportional increase in overall total pore volume is seen with respect to the SSA_{BET} in these microporous carbons.

Accordingly, the samples exhibit very different capacity trends for CO_2, H_2, H_2O and EDLC (**Figure 4d,e,f,** and Figures S9 and S10 in Supplementary Information). Specifically, the samples do not show further improved uptakes for CO_2 over UMCs (**Figure 2g** and Figure S9 in Supplementary Information). This is directly indicating the capacity distributions/inconsistencies trends appeared against the SSA_{BET} among the range of literature sorbents. From the data depicted in **Figure 2g** (Figure S9, Table S3 in Supplementary Information) it is obvious that the samples of higher surface areas, over 2000 $m^2\ g^{-1}$ are unlikely to yield further enhancement of uptake – in fact, more often they tend to show reduced uptakes. The reduced capacity trends can be understood from the high surface area GCs and MCs samples with a high proportion hierarchical pores or mesopores, shown in **Figure 4g,h**. Albeit having large SSA_{BET} and total pore volume, these samples show considerably lower capacities for both the CO_2 and EDLC (**Figure 4i,j, and Table 1**). Interestingly, no correlation is observed in their uptakes with respect to the SSA_{BET} or pore volumes at different pore-sizes, and is in line with other high surface area carbons in the literature (**Figure 2g,** and Figure S9 in Supplementary Information).

In addition to the superior CO_2 capacities of the UMCs among the reported carbons in the literature, the controlled pore size and distribution in our highly porous PMCs and CMCs also

exhibit noteworthy capacities for H_2 and H_2O (**Figure 2h,i**). The H_2 uptake capacities of around 3.0 wt% are relatively high with respect to similar surface area materials reported in the literature. Here it is worth noting here that many materials with SSA_{BET} of around 3000 $m^2\ g^{-1}$ reportedly exhibit uptakes of around 2.5 wt%.[8,12,29,31,36,42,43] Water vapour uptakes of up to 85 wt% are also form top capacities among the range porous solids.[44-48] These uptakes are higher than other carbon structures of similar surface area, and on par with zeolites and some of the functionalised MOFs and COFs.[44,45,48] For instance, the best example is commercial microporous carbon, BPL, which exhibits H_2O uptake of 40 wt% with SSA_{BET} of 1100 $m^2\ g^{-1}$. MOF-74 series samples of similar SSA_{BET} range, 1100-1250 $m^2\ g^{-1}$ show uptakes of 50-60 wt%. Carbons with a high degree of graphitic surfaces (or low-defect and therefore hydrophobic surfaces) often exhibit lower uptake capacities than the hydrophilic functional surfaces of doped structures.[44,46,48] Again, the structures with large pore-widths show decreased capacity.

The aqueous EDLC capacities between 300-320 $F\ g^{-1}$ at 500 $mA\ g^{-1}$ in our PMCs/CMCs with specific porosity characteristics outperform many of the other high surface area carbons (**Figures 3g, and 4f,** and Figures S9 and 10, Table S1 in Supplementary Information).[7,9,11,13,15-23,26,34,49-59] This clearly indicates that most of the samples with ultra-high porosity, for example the samples with SSA_{BET} greater than 2500 $m^2\ g^{-1}$, show reduced tendency in their EDLC values, and associated areal capacities are lower than 10 $\mu F\ cm^{-2}$ (**Figure 3f**). Our PMCs/CMCs with top gravimetric capacities simultaneously show impressive areal capacities, between 16-12 $\mu F\ cm^{-2}$. PMCs/CMCs also show excellent rate performance through their capacitance retention with respect to the increased current loads. As per comparative data represented in **Figure 4k**, these samples with SSA_{BET} of ≈2500 $m^2\ g^{-1}$ exhibit equally good rate and capacity performance with respect to the large number of

samples reported in the literature.[7,9,11,13,15-17,20,21,34,49-55] For example, micro-/mesoporous graphitic carbon, with SSA_{BET} of over 4000 $m^2 g^{-1}$, shows a capacitance value of just 225 F g^{-1} (and C_{SSA} of 5.5 µF cm^{-2}) at 0.5 A g^{-1}, far less than 320 or 270 F g^{-1} for the PMC450 or UMC450 with SSA_{BET} of 2500 or 1620 $m^2 g^{-1}$.[13] Hierarchical porous graphene carbon with SSA_{BET} >2500 $m^2 g^{-1}$ only show a capacitance value of 188 F g^{-1} (C_{SSA} = 7.5 µF cm^{-2}) at 1.0 A g^{-1}.[17] The high temperature carbonised MOFs and/or polymer impregnated MOF-templates with SSA_{BET} 2000-3000 $m^2 g^{-1}$ exhibit capacitance of 200-270 F g^{-1} with corresponding C_{SSA} value <10 µF cm^{-2}.[23] About 250 F g^{-1} is observed in the nitrogen-doped microporous carbons developed from carbonisation of MOFs for the surface area range 1000-2000 $m^2 g^{-1}$.[23] These are in good agreement with the capacities measured in our GCs and MCs. For instance, as shown in **Figures 3g and 4j** (Figure S9 in Supplementary Information), the activated graphene (GC-2) and carbonised MOF-5 (MC-2) with their high SSA_{BET} of 2780 and 2550 $m^2 g^{-1}$ as well as large mesopore volumes only show EDLC capacity of 220 and 190 F g^{-1}.

From the capacity trends depicted in **Figures 2g,h,i and 3g** (Figure S9 in Supplementary Information), it is very clear that the NPCs, with carefully controlled pore-widths and distribution, appear to form top values in all four cases studied (CO_2, H_2, H_2O and EDLC). For instance, the CO_2 capacities appear to reach maximum values for the surface area of about 2000 $m^2 g^{-1}$, any further increase in the SSA_{BET} do not deliver a proportional increase in their uptake, tends to show reduced capacities when SSA is increased beyond 2500 $m^2 g^{-1}$. In a similar way, the SSA_{BET} of about 2500 $m^2 g^{-1}$ is set as the optimum value for attaining the highest capacities for H_2, H_2O and EDLC (aqueous). As demonstrated with our PMCs/UMCs, as well as from the literature carbons, the high microporosity in the samples is controllable for a certain porosity range, which is mostly limited to SSA_{BET} around 1500-

2000 m^2 g^{-1} (**Figures 2, and 4, and Table 1**). Attempts made to further enhance the porosity in microporous samples; for example, surface areas greater than 2000 m^2 g^{-1}, has shown to develop mesoporosity at the expense of microporosity. Thus, samples of high porosity with surface areas higher than 2500 m^2 g^{-1} are concomitant with significant pore broadening and distribution across the micropore to mesopore region. Therefore, such samples show lower storage capacities than expected. From this one can also further understand the widely distributed capacities at a particular SSA_{BET}, and is directly attributed to their specific pore widths and related pore volumes.

The significantly improved EDLC and rate capacities in the PMCs/CMCs also result in high energy densities reaching to 7.0 Wh kg^{-1} at a power density of 500 W kg^{-1} (**Figure 4l**). Motivated by this performance, and given the controlled pore-widths in the samples the high voltage/energy supercapacitors (i.e., with a 2.7 V window compared to the 0.8 V in aqueous ones), using an organic electrolyte, are developed (**Figure 5** and Experimental details). The energy density of supercapacitors is governed by the operating voltage window (V) according to the energy (E) – capacitance (C) relation, $E = \frac{1}{2}CV^2$. CV and GCD curves in **Figure 5a,b,d,e** inform the EDLC behaviour, in good agreement with the literature.[58-77] This delivers very impressive EDLC capacities between 150-220 F g^{-1} at a high current density of 1.0 A g^{-1} along with rate performance. Due to their specific porosity characteristics, our CMCs/PMCs exhibit comparatively high capacitance to form top values among the numerous carbons in the literature. Here, it is worth noting that the EDLC capacity of ≈140 F g^{-1} at 1.0 A g^{-1} in our GC-2 (KOH activated GO, with large mesopore fraction) is in good agreement with the earlier reported values of 130-150 F g^{-1} from GO-based KOH activated carbons of similar porosity, thus validating the results.[17,75] The hierarchical porosity in MC-2 (MOF-5 derived carbon) with relatively high microporosity over GCs, results in enhanced EDLC

capacity of 170 F g^{-1}, which is also high compared to other similar surface area carbons in the literature. For example, the honeycomb-like porous carbon, is rich in specific 2-5 nm mesopores, with SSA_{BET} of 3500 m^2 g^{-1} delivers a capacity of 130 F g^{-1}.[62] Similarly, the mesoporeous carbon derived from asphalt/graphene composite achieves about 160 F g^{-1} for a SSA_{BET} of 3500 m^2 g^{-1}.[67] The templated mesoporous carbons from CDCs or polymers with SSA_{BET} of 2400-3200 m^2 g^{-1} yield capacity of 130-170 F g^{-1}.[17,69,72,77] Numerous samples with SSA_{BET} between 3000-3500 m^2 g^{-1} show capacities between 130-200 F g^{-1} (**Figure 5g, Table 1,** and Table S2 in Supplementary Information). Montmorillonite confined gelatin derived carbon with SSA_{BET} of 2770 m^2 g^{-1} (where mesopore volume is contributing to 66% of the total pore volume) yields a lower capacitance of 106 F g^{-1}.[11] Commercial activated carbons with high SSA_{BET} of 2000-2400 m^2 g^{-1} deliver ≈100-140 F g^{-1}.[61] As shown in **Figure 5h,i,** due to the controlled porosity in our PMCs/CMCs samples the supercapacitors readily deliver exceptional energy densities between 40-51 Wh kg^{-1} at a relatively high power density of 1000 W kg^{-1}, as well as impressive rate performance over numerous literature carbons (**Table 1,** and Table S2 in Supplementary Information). All these results clearly show that the capacities are enhanced by controlling the pore-widths and pore distribution across the microporous and near mesoporous regions.

The five case studies (CO_2, H_2, H_2O and EDLC in aqueous and organic electrolyte) suggest that apart from the SSA_{BET}, the pore volume, particularly at relevant pore-widths plays a critical role in enhancing the capacity. This is further schematically depicted in **Figure 6**. The pores matching the guest molecule/ion size can yield high adsorptive density. It has been shown that in sub-nanometre sized pores the guest molecules/ions experience overlapping potentials (dispersion interactions or Lennard-Jones 6-12 potentials) from both the walls and the small pore channels also promote the strong adsorbate-adsorbate interactions, in addition

to adsorbent-adsorbate (known as cooperative adsorption).[6] All these ultimately create a high adsorbed density within the pore volume that is equivalent to the density of the bulk fluid. The pore-sizes that can accommodate two-layers of adsorbates yield maximum pore utilisation to attain efficient capacities proportional to their porosity/surface area (**Figure 6a**). Whereas, a gradually decreased adsorption density is expected with larger pore-widths, since the adsorbate-adsorbent interaction/potentials tend to weaken from the first adsorption layer to subsequent adsorbates (**Figure 6b,c,d**). In additions to pore-size, the types of pores also show a promising effect on the adsorption capacities. For instance, the slit-pores exhibit relatively high adsorption capacity as these can offer more surface area and strong binding from overlapping potentials than cylindrical and spherical pores (**Figure 6e**). Note that on a per unit pore volume basis the cylindrical and spherical pores offers reduced surface area for adsorption.

Among the applications, it is found that sufficiently high ultramicroporosity (at ≤1.0 nm pore widths) is required for large CO_2 uptake. Whereas, in the case of water or aqueous supercapacitor, the controlled pore widths in the region ≤1.5 nm appears to show the highest capacity. In addition to the specific porosities, the functionalised pore surfaces, for instance, the pore surface defects and oxygen or other heteroatom functional groups or metal-centres, have shown to boost the overall uptakes. It has been shown that nitrogen or certain other heteroatom doped structures create heterogeneous surfaces to provide more binding sites density for attracting guest molecules/ions. Functionalities like N-atoms can increase the basicity of the carbon structure, which in turn will anchor the electron-deficient C-atom of the CO_2 to pore surface via Lewis-acid/Lewis-base interactions. This effect can be further understood from the CO_2 uptakes normalized to the surface areas (**Figure 2g**).[5,23] Similarly, the oxygen functional groups in the pore space would also enhance the CO_2, water and

capacitance in aqueous electrolytes by forming hydrogen bonds/wettability. It has been shown that water forms three-dimensional clusters centred on functional groups instead of layer by layer adsorption.[46] These adsorbed water molecules act like new active sites and host new water molecules that readily form a bridge instead of pore-filling. High ultra microporosity and oxygen functionalities both favour the above mentioned process and facilitate progressive adsorption with respect to time. The slightly slower water uptake kinetics can be associated with the time delay involved in formation of the water bridge of larger sized pores; for example, UMC350 to UMC450 (**Figure 2f**). It has also been proposed that such surface functionality or heterogeneity contribute to the pseudocapacitance via chemical redox reactions to enhance the overall capacitance.[58,59] It has been established that nitrogen, and certain other heteroatom and transition-metal related dopants, such as hydroxides, oxides, sulphides, nitrides, etc. in the carbons create charged (heterogeneous) surface regions which enable the redox reactions to contribute to the overall capacitance, i.e., via pseudocapacitance. Here it is worth noting that all of the samples reported in this work are free from heteroatom functionalities, except inherent/activation assisted incorporation of oxygen and defective carbon functionalities.

Furthermore, as depicted in **Figure 6f,g,h**, the precursors and processing methods yield different pore-types in their NPCs. The biomass, pine-cones and coffee-grounds under low concentration of KOH activation yield highly microporous carbons, with pore-sizes distributed under 1.0 and 2.0 nm pore-widths, with a small fraction less than 3.0 nm (**Figures 2a,b,c, 4a,b,c, and 6f**). The direct carbonisation of MOFs as sacrificial templates preserves their initial porosity between 1-2 nm pore-widths, which are of the cylindrical and spherical types (**Figures 4h, and 6g**). Slit and large pores develop at the expense of framework collapse and inherent metal clustering to form as large porogenes.[23-25,41] The GO-based

structures yield slit and mesopores due to their layer assembly and large amount of potassium complex intercalation as porogenes (**Figures 4h, and 6h**).[6,17,40,74,75] Thus, the UMCs and controlled pore-widths in PMCs and CMCs should offer efficient pore utilisation to achieve higher adsorptive capacities than other highly porous GCs and MCs with relatively large pore-widths. Here it is worth noting that high surface area carbons and other solids, such as MOFs, CPs are always concomitant with large pore-sizes resulting in reduced capacities due to the weak physisorption, as well as inefficient charge separation and distribution in case of EDLCs. It is important to note that all the capacities related to CO_2, H_2, H_2O, and EDLC are fundamentally directed by physisorption.

Conclusion

Targeted synthesis of nanoporous carbons and their efficient multifunctional performance for storing gas/vapour/liquid molecules and electric charges is demonstrated for five case studies; CO_2, H_2, H_2O and EDLC supercapacitors in aqueous and organic electrolytes, for the first time. The initial precursor types and processing provides good control over the expected porosity in the final products. Under such a controlled synthesis process, the UMCs exhibit over 91% of the total porosity from pores with sizes well below 1.0 nm. Then the specifically designed microporous carbons, from pine-cones and coffee-grounds, exhibit high porosity characteristics under controlled pore-widths with surface areas and pore volumes reaching to 2600 $m^2\ g^{-1}$ and 0.90 $cm^3\ g^{-1}$. The graphene-oxide and MOFs-based NPCs reveal further extended porosities across micro-/mesoporous region. Thus, under optimised porosity the NPCs exhibit significantly enhanced capacities for all five case studies. Specifically, the capacities, ≈8.0 mmol $g^{-1}$of CO_2, 3.0 wt% of H_2, 85 wt% of H_2O, and 320 F g^{-1} (or >16 µF cm^{-2}) and 230 g^{-1} of EDLC in aqueous and organic electrolyte with 51 Wh kg^{-1} of energy density, in the NPCs of controlled pore-widths are forming the top values among the

numerous existing carbons of wide range porosities in the literature. Here it is worth noting that the samples of very high porosity with a surface area greater than 2500 $m^2 g^{-1}$ are unlikely to exhibit improved capacities, and in fact show reduced uptakes. Therefore, this work provides useful guidelines; limitations and further insights in the development of carbon nanostructures under efficient production routes and for multifunctional energy storage application.

Experimental

Synthesis: Pines cones were collected from around the University of East Anglia, Norwich campus, and thoroughly washed in distilled water followed by drying at 80 °C in a vacuum oven overnight. They were then subjected to carbonisation at different temperatures between 250 °C and 550 °C for an hour, under nitrogen flow in a horizontal tube furnace with a heating rate of 5 °C per minute. The samples were named as biochars: BC250, BC350, BC450, and BC550 with respect to the carbonisation temperature of 250 °C, 350 °C, 450 °C, and 550 °C. Each biochar sample was ground and then mixed with 30 ml distilled water and potassium hydroxide (KOH, pellets of ≥85 % purity, Sigma Aldrich) in a mass ratio of 1:3 biochar to KOH, followed by stirring at 70 °C until dried. Each composite was activated in a horizontal tube furnace at 750 °C for an hour, at a heating rate of 5 °C per minute, and under nitrogen gas flow. The resultant activated carbon samples were subsequently washed with 25 ml 0.1 M hydrochloric acid, followed by distilled water until the washings were pH neutral. The final samples are named as UMC250, UMC350, UMC450 and UMC550, respectively, according to their precursor biochars - BC250, BC350, BC450, and BC550. All the activated samples were handled in air for all further characterisation.

The highly porous carbons are synthesised as follows. Biochars of pine-cones and coffee-grounds obtained at carbonising between 350-650 °C were ground to fine powders and mixed

with KOH in a 1: 3 mass ratio of chars to KOH in DI water and left stirred at least overnight. Then the dried samples were subjected to activation at 750 °C for an hour under nitrogen atmosphere. The obtained microporous carbons from pine-cones and coffee-grounds respectively are named as PMC-x and CMC-x, where –x represents the biochar temperature. For example, the pine-cones/coffee-grounds carbonised at 650 °C followed by KOH activation is named as PMC-650/CMC-650. The precursors, graphene-oxide (GO), and MOF-5 were synthesised and processed according to earlier reports.[6,24,25,30,75] Briefly, the GC-1 and GC-2 samples were obtained by activating at 800 °C with the different GO precursors and KOH blending methods from 1:6 GO to KOH mass ratios in solid-state mixture, and thermal-shock exfoliated GO in 7 M KOH solution, respectively.[6,24,30,75] MCs were synthesised via direct carbonisation at 900 and 1000 °C without the use of KOH or chemical activation or further washing and are names as MC-1 and MC-2, respectively.[23,25]

Characterisation: Powder X-Ray diffraction (PXRD, on Thermo Scientific Equinox 3000, Cu Kα radiation) was carried out in the scan range of 2θ = (3-80)° and step size of 0.01°. Raman spectra were recorded with a ×50 microscope using a 514.5 nm laser on a Renishaw inVia spectrometer. X-ray photoemission spectroscopy (XPS, Al-K-alpha, Thermo Scientific) data, scanning electron microscopy (SEM, Jeol) and transmission electron microscopy (TEM, Jeol) measurements were carried out on the samples supported on a carbon tape or a carbon-coated copper TEM grid. Thermogravimetry (Setsys, Setaram) was carried out up to 800 °C with a heating rate of 5 °C per minute on a dry sample under Ar flow.

Porosity (N_2), and H_2, CO_2 and H_2O uptake measurements: All gases used were research grade purity, purchased from BOC, UK. The porosity (by N_2 as a probe molecule) and gas (H_2 and CO_2) adsorption-desorption isotherms in the pressure range of vacuum to 1 bar were measured at 77 K (for N_2 and H_2) and 273 K (for CO_2) using a Quantachrome Autosorb-iQC. The specific surface area was determined from the N_2 isotherm, according to the Brunauer-

Emmett-Teller (BET) method. QSDFT (quenched solid density functional theory) method with slit/cylindrical pores was applied to obtain a pore-size distribution, micropore volume and cumulative pore volume. The ultra-micropore-size distribution below 1.0 nm was deduced from NLDFT (non-local density functional theory) fitting to 273 K CO_2 adsorption isotherms. Both the QSDFT and NLDFT models used were available within in the Quantachrome ASiQwin isotherm analysis software. The total pore volume was estimated from the amount of N_2 adsorbed at a relative pressure, $P\,P_0^{-1}$ of ≈0.95. For all N_2, H_2, and CO_2 uptake data, the samples were initially degassed at 180 °C for up to 24 h prior to the actual adsorption isotherm measurements. Gravimetric water uptake and kinetics tests were carried out on a thermogravimetric analyser under a constant gas flow bubbled through a water bubbler at 100 ml min^{-1} around 1 bar and room temperature, with a relative humidity of ≥85%. These tests were carried out after the samples were treated at 200 °C to remove the residual moisture under dry argon gas. Water uptake capacity at different humidity levels between 35% RH and 100% RH were determined by weight gain of the samples (from their vacuum outgassed dry weights) using a 0.01 mg accuracy balance. The lower humidity data was recorded at different times/days by leaving open sample vials in the laboratory atmosphere, whereas 100%RH was achieved by keeping the sample vials next to the water bath and closed system.

Supercapacitor fabrication and testing: Working electrodes were prepared by mixing the active carbon material (2.00 mg for dry weight by considering the ultra-porous capillary action for moisture adsorption of 30-40 wt%) with additional 10 wt% PTFE (adjusted from diluting the as-received 60 wt% dispersion in water, Sigma Aldrich) and ethanol until paste-like, using an agate mortar and pestle, followed by transfering the paste as a thinfilm onto the current collector (nickel foam discs of 10 mm diameter). The nickel foam discs were cut from sheet (battery grade from MTI corp.) and then treated with 30% HCl for 5 minutes in an

ultrasonication bath to remove factory/shipping contaminations and surface oxidation, followed by washing and drying. The active carbon-coated electrodes were dried at 60 °C for a couple of hours and compressed at 0.7 ton using a pelletiser. The mass loading of samples in the electrodes is in the range of 2-3 mg cm^{-2}. The symmetric supercapacitor was fabricated by the assembly of two working electrodes and a cellulose membrane separator into a sandwich-like structure in a stainless-steel split flat cell (MTI corp.) along with the electrolyte (6.0 M KOH) at ambient conditions. The dried electrodes were left soaked in the intended electrolyte at least overnight to 24 h before being subjected to electrochemical tests. For organic electrolyte (1.0 M $TEABF_4$ in acetonitrile), carbon paper (Fuel Cell Store) discs were used as the current collectors. The active electrode was prepared using a similar method as that of the aqueous capacitors and coated on to the current collectors. As the organic electrolyte is air/moisture sensitive, the electrodes were dried at 120 °C under vacuum overnight. The symmetric supercapacitiors were assembled using with a Celgard separator in an argon-filled glove box (from MBRAUN) with oxygen and mositure levels at <0.1 ppm. All electrochemical tests were carried out using an Autolab (Metrohm PGSTAT302N) electrochemical workstation, by a two-electrode method on symmetric supercapacitors at room temperature. Before actual measurements, the supercapacitor was subjected to a number of CV (cyclic voltammetry) cycles at a scan rate of 50 mV s^{-1} until stable and superimposed CV curves were obtained. Actual CV tests were conducted at different scan rates between (5 and 500) mV s^{-1} in a fixed voltage range of 0.0 V to 0.8 V. The charge-discharge curves with respective upper and lower cut-off voltages were recorded at a wide range of discrete applied current densities between (0.1 and 25) A g^{-1}, on single electrode, 2.00 mg active material-base. Long-term cyclic stability tests were conducted with multiple charge-discharge cycles up to several thousands of cycles at a constant applied current density of 5 A g^{-1}. Specific gravimetric capacitance C (F g^{-1}), was calculated from GCD

curves according to: $C = 4(I \times \Delta t)/(m \times \Delta V)$, where I is the discharge current (A); m is the total mass of active material on both the electrodes (g); Δt is the discharge time (s) and ΔV is the operating voltage (V); the factor 4 is related to normalisation to the mass of one electrode for the two identical capacitors in series. The specific capacitance from CV was calculated using the following equation: $C = 4(Area\ of\ CV\ loop)/(2m \times s \times \Delta V)$, where s is the voltage scan rate (dV/dt) and ΔV corresponds to the potential window of the CV. The gravimetric energy density of two electrodes in a device were derived by: E_{wt} (Wh kg^{-1}) = [($C_{wt} \times \Delta V^2$)/8] × (1000/3600). The corresponding power density was obtained from: P_{wt} (W kg^{-1}) = ($E_{wt}/\Delta t$) × 3600.[58]

Conflicts of interest

There are no conflicts of interest to declare

Supporting Information

Supporting Information is available from the Wiley Online Library or from the author.

Acknowledgements

This work was supported by the EPSRC (EP/R023581/1; EP/S018204/2; EP/P009050/1, EP/N032888/1, EP/M009394/1); Brett and Shearing acknowledge the Faraday Institution for supporting energy storage research in the Electrochemical Innovation Lab (549585, 547601) and Shearing the Royal Academy of Engineering.

References

[1] W.-J. Liu, H. Jiang, H.-Q. Yu, Emerging applications of biochar-based materials for energy storage and conversion, *Energy Environ. Sci.*, 2019, 12, 1751-1779.

[2] H. Jin, J. Li, Y. Yuan, J. Wang, J. Lu, S. Wang, Recent progress in biomass-derived electrode materials for high volumetric performance supercapacitors, *Adv. Energy Mater.*, 2018, 8, 1801007.

[3] Z. Zhang, Z. P. Cano, D. Luo, H. Dou, A. Yu, Z. Chen, Rational design of tailored porous carbon-based materials for CO2 capture, *J. Mater. Chem. A*, 2019, 7, 20985-21003.

[4] Z. Bi, Q. Kong, Y. Cao, G. Sun, F. Su, X. Wei, X. Li, A. Ahmad, L. Xie, C.-M. Chen, Biomass-derived porous carbon materials with different dimensions for supercapacitor electrodes: a review, *J. Mater. Chem. A*, 2019, 7, 16028-16045.

[5] G. Singh, K. S. Lakhi, S. Sil, S. V. Bhosale, I. Y. Kim, K. Albahily, A. Vinu, Biomass derived porous carbon for CO_2 capture, *Carbon*, 2019, 148, 164-186.

[6] S. Gadipelli, Z. X. Guo, Graphene-based materials: synthesis and gas sorption, storage and separation, *Prog. Mater. Sci.*, 2015, 69, 1-60.
[7] D. Li, G. Chang, L. Zong, P. Xue, Y. Wang, Y. Xia, C. Lai, D. Yang, From double-helix structured seaweed to S-doped carbon aerogel with ultra-high surface area for energy storage, *Energy Storage Mater.*, 2019, 17, 22-30.
[8] T. S. Blankenship, R. Mokaya, Cigarette butt-derived carbons have ultra-high surface area and unprecedented hydrogen storage capacity, *Energy Environ. Sci.*, 2017, 10, 2552-2562.
[9] X. Zhou, P. Wang, Y. Zhang, L. Wang, L. Zhang, L. Zhang, L. Xu, and L. Liu, Biomass based nitrogen-doped structure-tunable versatile porous carbon materials, *J. Mater. Chem. A*, 2017, 5, 12958-12968.
[10] K. Li, S. Tian, J. Jiang, J. Wang, X. Chen, F. Yan, Pine cone shell-based activated carbon used for CO_2 adsorption, *J. Mater. Chem. A*, 2016, 4, 5223-5234.
[11] X. Fan, C. Yu, J. Yang, Z. Ling, C. Hu, M. Zhang, J. Qiu, A layered-nanospace-confinement strategy for the synthesis of two-dimensional porous carbon nanosheets for high-rate performance supercapacitors, *Adv. Energy Mater.*, 2015, 5, 1401761.
[12] J.-S. M. Lee, M. E. Briggs, T. Hasell, A. I. Copoper, Hyperporous carbons from hypercrosslinked polymers, *Adv. Mater.*, 2016, 28, 9804-9810.
[13] J. W. F. To, Z. Chen, H. Yao, J. He, K. Kim, H.-H. Chou, L. Pan, J. Wilcox, Y. Cui, Z. Bao, Ultrahigh surface area three-dimensional porous graphitic carbon from conjugated polymeric molecular framework, *ACS Cent. Sci.*, 2015, 1, 68-76.
[14] A. Silvestre-Albero, J. Silvestre-Albero, M. Martínez-Escandell, F. Rodríguez-Reinoso, Micro/mesoporous activated carbons derived from polyaniline: promising candidates for CO_2 adsorption, *Ind. Eng. Chem. Res.*, 2014, 53, 15398-15405.
[15] Y. Li, Y. Liang, H. Hu, H. Dong, M. Zheng, Y. Xiao, Y. Liu, KNO_3-mediated synthesis of high-surface-area polyacrylonitrile-based carbon material for exceptional supercapacitors, *Carbon*, 2019, 152, 120-127.
[16] J. Huang, Y. Liang, H. Hu, S. Liu, Y. Cai, H. Dong, M. Zheng, Y. Xiao, Y. Liu, Ultrahigh-surface-area hierarchical porous carbon from chitosan: acetic acid mediated efficient synthesis and its application in superior supercapacitors, *J. Mater. Chem. A*, 2017, 5, 24775-24781.
[17] J. Xu, Z. Tan, W. Zeng, G. Chen, S. Wu, Y. Zhao, K. Ni, Z. Tao, M. Ikram, H. Ji, Y. Zhu, A Hierarchical carbon derived from sponge-templated activation of graphene oxide for high-performance supercapacitor electrodes, *Adv. Mater.*, 2016, 28, 5222-5228.
[18] J. Zhou, Z. Li, W. Xing, H. Shen, X. Bi, T. Zhu, Z. Qiu, S. Zhuo, A new approach to tuning carbon ultramicropore size at sub-angstrom level for maximizing specific capacitance and CO_2 uptake, *Adv. Funct. Mater.*, 2016, 26, 7955-7964.
[19] M. Liu, J. Qian, Y. Zhao, D. Zhu, L. Gan, L. Chen, Core-shell ultramicroporous@microporous carbon nanospheres as advanced supercapacitor electrodes, *J. Mater. Chem. A*, 2015, 3, 11547-11526.
[20] J. Zhao, H. Lai, Z. Lyu, Y. Jiang, K. Xie, X. Wang, Q. Wu, L. Yang, Z. Jin, Y. Ma, J. Liu, Z. Hu, Hydrophilic hierarchical nitrogen-doped carbon nanocages for ultrahigh supercapacitive performance, *Adv. Mater.*, 2015, 27, 3541-3545.
[21] F. Xu, Z. Tang, S. Huang, L. Chen, Y. Liang, W. Mai, H. Zhong, R. Fu, D. Wu, Facile synthesis of ultrahigh-surface-area hollow carbon nanospheres for enhanced adsorption and energy storage, *Nat. Comm.*, 2015, 6, 7221.
[22] B. Xu, S. Hou, H. Duan, G. Cao, M. Chu, Y. Yang, Ultramicroporous carbon as electrode material for supercapacitors, *J. Power Sour.*, 2013, 228, 193-197.

[23] S. Gadipelli, Z. Li, Y. Lu, J. Li, J. Guo, N. T. Skipper, P. R. Shearing, D. J. L. Brett, Size-related electrochemical performance in active carbon nanostructures: a MOFs-derived carbons case study, *Adv. Sci.*, 2019, 6, 1901517.
[24] S. Gadipelli, H. A. Patel, Z. Guo, An ultrahigh pore volume drives up the amine stability and cyclic CO_2 capacity of a solid-amine@carbon sorbent, *Adv. Mater.*, 2015, 27, 4903-4909.
[25] G. Srinivas, V. Krungleviciute, Z.-X. Guo, T. Yildirim, Exceptional CO_2 capture in a hierarchically porous carbon with simultaneous high surface area and pore volume, *Energy Environ. Sci.*, 2014, 7, 335-342.
[26] C. R. Pérez, S.-H. Yeon, J. Ségalini, V. Presser, P.-L. Taberna, P. Simon, Y. Gogotsi, Structure and electrochemical performance of carbide-derived carbon nanopowders, *Adv. Funct. Mater.*, 2013, 23, 1081-1089.
[27] V. Presser, J. McDonough, S.-H. Yeon, Y. Gogotsi, Effect of pore size on carbon dioxide sorption by carbide derived carbon, *Energy Environ. Sci.*, 2011, 4, 3059-3066.
[28] Y. Xia, R. Mokaya, G. S. Walker, Y. Zhu, Superior CO_2 adsorption capacity on N-doped, high-surface-area, microporous carbons templated from zeolite, *Adv. Energy Mater.*, 2011, 1, 678-683.
[29] C. Ge, J. Song, Z. Qin, J. Wang, W. Fan, Polyurethane foam-based ultramicroporous carbons for CO_2 capture, *ACS Appl. Mater. Interfaces*, 2016, 8, 18849-18859.
[30] S. Gadipelli, Y. Lu, N. T. Skipper, T. Yildirim, Z. Guo, Design of hyperporous graphene networks and their application in solid-amine based carbon capture systems, *J. Mater. Chem. A*, 2017, 5, 17833-17840.
[31] Y. Wang, X. Chen, Q.-G. Zhai, J. Guo, P. Feng, Ultraporous nitrogen-rich carbon nanosheets derived from the synergy of eutectic liquid and zeolitic imidazolate for energy applications, *J. Power Sour.*, 2019, 434, 126678.
[32] J. Li, B. Michalkiewicz, J. Min, C. Ma, X. Chen, J. Gong, E. Mijowska, T. Tang, Selective preparation of biomass-derived porous carbon with controllable pore sizes toward highly efficient CO_2 capture, *Chem. Eng. J.*, 2019, 360, 250-259.
[33] H. Sun, B. Yang, A. Li, Biomass derived porous carbon for efficient capture of carbon dioxide, organic contaminants and volatile iodine with exceptionally high uptake, *Chem. Eng. J.*, 2019, 372, 65-73.
[34] H. Wei, J. Chen, N. Fu, H. Chen, H. Lin, S. Han, Biomass-derived nitrogen-doped porous carbon with superior capacitive performance and high CO_2 capture capacity, *Electrochim. Acta*, 2018, 266, 161-169.
[35] A.-Z. Peng, S.-C. Qi, X. Liu, D.-M. Xue, S.-S. Peng, G.-X. Yu, X.-Q. Liu, L.-B. Sun, N-doped porous carbons derived from a polymer precursor with a record high N content: efficient adsorbents for CO_2 capture, *Chem. Eng. J.*, 2019, 372, 656-664.
[36] W. Sangchoom, R. Mokaya, Valorization of Lignin Waste: carbons from hydrothermal carbonization of renewable lignin as superior sorbents for CO_2 and hydrogen storage, *ACS Sustainable Chem. Eng.*, 2015, 3, 1658-1667.
[37] G. Sethia, A. Sayari, Comprehensive study of ultra-microporous nitrogen-doped activated carbon for CO_2 capture, *Carbon*, 2015, 93, 68-80.
[38] Ashourirad B, Sekizkardes A K, Altarawneh S, El-Kaderi H. M., Exceptional gas adsorption properties by nitrogen-doped porous carbons derived from benzimidazole-linked polymers, *Chem. Mater.*, 2015, 27, 1349-1358.
[39] J. Chen, J. Yang, G. Hu, X. hu, Z. Li, S. Shen, M. Radosz, M. Fan, Enhanced CO_2 capture capacity of nitrogen-doped biomass-derived porous carbons, *ACS Sustainable Chem. Eng.*, 2016, 4, 1439-1445.

[40] W. Travis, S. Gadipelli, Z. Guo, Superior CO_2 adsorption from waste coffee ground derived carbons, *RSC Adv.*, 2015, 5, 29558-29562.
[41] S. Gadipelli, Z. X. Guo, Tuning of ZIF-derived carbon with high activity, nitrogen functionality, and yield – a case for superior CO_2 capture, *ChemSusChem*, 2015, 8, 2123-2132.
[42] N. Balahmar, R. Mokaya, Pre-mixed precursors for modulating the porosity of carbons for enhanced hydrogen storage: towards predicting the activation behaviour of carbonaceous matter, *J. Mater. Chem. A*, 2019, 7, 17466-17479.
[43] D. Wang, Y. Shen, Y. Chen, L. Liu, Y. Zhao, Microwave-assistant preparation of N/S co-doped hierarchical porous carbons for hydrogen adsorption, *Chem. Eng. J.*, 2019, 367, 260-268.
[44] Y. Byun, S. H. Je, S. N. Talapaneni, A. Coskun, Advances in porous organic polymers for efficient water capture, *Chem. Eur. J.*, 2019, 25, 10262-10283.
[45] N. Ogiwara, H. Kobayashi, P. Concepciln, F. Rey, H. Kitagawa, The first study on the reactivity of water vapor in metal–organic frameworks with platinum nanocrystals, *Angew. Chem. Int. Ed.*, 2019, 58, 11731-11736.
[46] L. Liu, S. Tan, T. Horikawa, D.D. Do, D. Nicholson, J. Liu, Water adsorption on carbon - a review, *Adv. Colloid Interface Sci.*, 2017, 250, 64-78.
[47] L. F. Velasco, R. Guillet-Nicolas, G. Dobos, M. Thommes, P. Lodewyckx, Towards a better understanding of water adsorption hysteresis in activated carbons by scanning isotherms, *Carbon*, 2016, 96, 753-758.
[48] H. Furukawa, F. Gándara, Y.-B. Zhang, J. Jiang, W. L. Queen, M. R. Hudson, O. M. Yaghi, Water adsorption in porous metal−organic frameworks and related materials, *J. Am. Chem. Soc.*, 2014, 136, 4369-4381.
[49] Z. Chen, X. Wang, B. Xue, Q. Wei, L. Hu, Z. Wang, X. Yang, J. Qiu, Self-templating synthesis of 3D hollow tubular porous carbon derived from straw cellulose waste with excellent performance for supercapacitors, *ChemSusChem*, 2019, 12, 1390-1400.
[50] C. Kim, C. Zhu, Y. Aoki, H. Habazaki, Heteroatom-doped porous carbon with tunable pore structure and high specific surface area for high performance supercapacitors, *Electrochim. Acta*, 2019, 314, 173-187.
[51] G. Yuan, Y. Liang, H. Hu, H. Li, Y. Xiao, H. Dong, Y. Liu, M. Zheng, Extraordinary thickness-independent electrochemical energy storage enabled by cross-linked microporous carbon nanosheets, *ACS Appl. Mater. Interfaces*, 2019, 11, 26946-26955.
[52] N. Diez, G. A. Ferrero, M. Sevilla, A. B. Fuertes, A sustainable approach to hierarchically porous carbons from tannic acid and their utilization in supercapacitive energy storage systems, *J. Mater. Chem. A*, 2019, 7, 14280-14290.
[53] W. Sangchoom, D. A. Walsh, R. Mokaya, Valorization of lignin waste: high electrochemical capacitance of lignin-derived carbons in aqueous and ionic liquid electrolytes, *J. Mater. Chem. A*, 2018, 6, 18701-18711.
[54] S. Dong, X. He, H. Zhang, X. Xie, M. Yu, C. Yu, N. Xiao, J. Qiu, Surface modification of biomass-derived hard carbon by grafting porous carbon nanosheets for high-performance supercapacitors, *J. Mater. Chem. A*, 2018, 6, 15954-15960.
[55] L. Pan, Y. Wang, H. Hu, X. Li, J. Liu, L. Guan, W. Tian, X. Wang, Y. Li, M. Wu, 3D self-assembly synthesis of hierarchical porous carbon from petroleum asphalt for supercapacitors, *Carbon*, 2018, 134, 345-353.
[56] B. Lobato, L. Suarez, L. Guardia, T. A. Centeno, Capacitance and surface of carbons in supercapacitors, *Carbon*, 2017, 122, 434-445.

[57] H. Ji, X. Zhao, Z. Qiao, J. Jung, Y. Zhu, Y. Lu, L. L. Zhang, A. H. MacDonald, R. S. Ruoff, Capacitance of carbon-based electrical double-layer capacitors, *Nat. Comm.*, 2014, 5, 3317.
[58] F. Beguin, V. Presser, A. Balducci, and E. Frackowiak, Carbons and electrolytes for advanced supercapacitors, *Adv. Mater.*, 2014, 26, 2219-2251.
[59] M. Sevilla, R. Mokaya, Energy storage applications of activated carbons: supercapacitors and hydrogen storage, *Energy Environ. Sci.*, 2014, 7, 1250-1280.
[60] J. Xu, N. Yuan, J. M. Razal, Y. Zheng, X. Zhou, J. Ding, K. Cho, S. Ge, R. Zhang, Y. Gogotsi, R. H. Baughman, Temperature-independent capacitance of carbon-based supercapacitor from −100 to 60 °C, *Energy Storage Mater.*, 2019, 22, 323-329.
[61] C. Schütter, S. Pohlmann, A. Balducci, Industrial requirements of materials for electrical double layer capacitors: impact on current and future applications, *Adv. Energy Mater.*, 2019, 9, 1900334.
[62] T. Guan, J. Zhao, G. Zhang, J. Wang, D. Zhang, K. Li, Template-free synthesis of honeycomblike porous carbon rich in specific 2−5 nm mesopores from a pitch-based polymer for a high-performance supercapacitor, *ACS Sustainable Chem. Eng.*, 2019, 7, 2116-2126.
[63] K. Liu, X. Zheng, K. Wang, C. Wang, M. Chen, Sodium metal-assisted carbonization of pyrrole to prepare N-doped porous carbons for high-rate performance supercapacitors, *Carbon*, 2019, 153, 265-273.
[64] V. Sattayarut, T. Wanchaem, P. Ukkakimapan, V. Yordsri, P. Dulyaseree, M. Phonyiem, M. Obata, M. Fujishige, K. Takeuchi, W. Wongwiriyapan, M. Endo, Nitrogen self-doped activated carbons via the direct activation of Samanea saman leaves for high energy density supercapacitors, *RSC Adv.*, 2019, 9, 21724-21732.
[65] Qi, Z. Xia, R. Sun, X. Sun, X. Xu, W. Wei, S. Wang, G. Sun, Graphitization induced by KOH etching for the fabrication of hierarchical porous graphitic carbon sheets for high performance supercapacitors, *J. Mater. Chem. A*, 2018, 6, 14170-14177.
[66] P. Chang, C. Wang, T. Kinumoto, T. Tsumura, M. Chen, M. Toyoda, Frame-filling C/C composite for high-performance EDLCs with high withstanding voltage, *Carbon*, 2018, 131, 184-192.
[67] M. Zhang, Z. Sun, T. Zhang, B. Qin, D. Sui, Y. Xie, Y. Ma, Y. Chen, Porous asphalt/graphene composite for supercapacitors with high energy density at superior power density without added conducting materials, *J. Mater. Chem. A*, 2017, 5, 21757-21764.
[68] Y. Lu, S. Zhang, J. Yin, C. Bai, J. Zhang, Y. Li, Y. Yang, Z. Ge, M. Zhang, L. Wei, M. Ma, Y. Ma, and Y. Chen, Mesoporous activated carbon materials with ultrahigh mesopore volume and effective specific surface area for high performance supercapacitors, *Carbon*, 2017, 124, 64-71.
[69] H. Zhou, Y. Peng, H. B.Wub, F. Sun, H. Yu, F. Liu, Q. Xu, Y. Lu, Fluorine-rich nanoporous carbon with enhanced surface affinity inorganic electrolyte for high-performance supercapacitors, *Nano Energy*, 2016, 21, 80-89.
[70] W. Sun, S. M. Lipka, C. Swartz, D. Williams, Fuqian Yang, Hemp-derived activated carbons for supercapacitors, *Carbon*, 2016, 103, 181-192.
[71] D. Kang, Q. Liu, J. Gu, Y. Su, W. Zhang, D. Zhang, "Egg-Box"-assisted fabrication of porous carbon with small mesopores for high-rate electric double layer capacitors, *ACS Nano*, 2015, 9, 11225-11233.
[72] G. A. Ferrero, A. B. Fuertes, M. Sevilla, N-doped microporous carbon microspheres for high volumetric performance supercapacitors, *Electrochim. Acta*, 2015, 168, 320-329.

[73] M. Sevilla, A. B. Fuertes, Direct synthesis of highly porous interconnected carbon nanosheets and their application as high-performance supercapacitors, *ACS Nano*, 2014, 8, 5069-5078.
[74] L. Zhang, F. Zhang, X. Yang, G. Long, Y. Wu, T. Zhang, K. Leng, Y. Huang, Y. Ma, A. Yu, Y. Chen, Porous 3D graphene-based bulk materials with exceptional high surface area and excellent conductivity for supercapacitors, *Sci. Rep.*, 2013, 3, 1408.
[75] Y. Zhu, S. Murali, M. D. Stoller, K. J. Ganesh, W. Cai, P. J. Ferreira, A. Pirkle, R. M. Wallace, K. A. Cychosz, M. Thommes, D. Su, E. A. Stach, R. S. Ruoff, Carbon-based supercapacitors produced by activation of graphene, *Science*, 2011, 332, 1537-1541.
[76] L. Wei, M. Sevilla, A. B. Fuertes, R. Mokaya, G. Yushin, Hydrothermal carbonization of abundant renewable natural organic chemicals for high-performance supercapacitor electrodes, *Adv. Energy Mater.*, 2011, 1, 356-361.
[77] Y. Korenblit, M. Rose, E. Kockrick, L. Borchardt, A. Kvit, S. Kaskel, G. Yushin, High-rate electrochemical capacitors based on ordered mesoporous silicon carbide-derived carbon, *ACS Nano*, 2010, 4, 1337-1344.

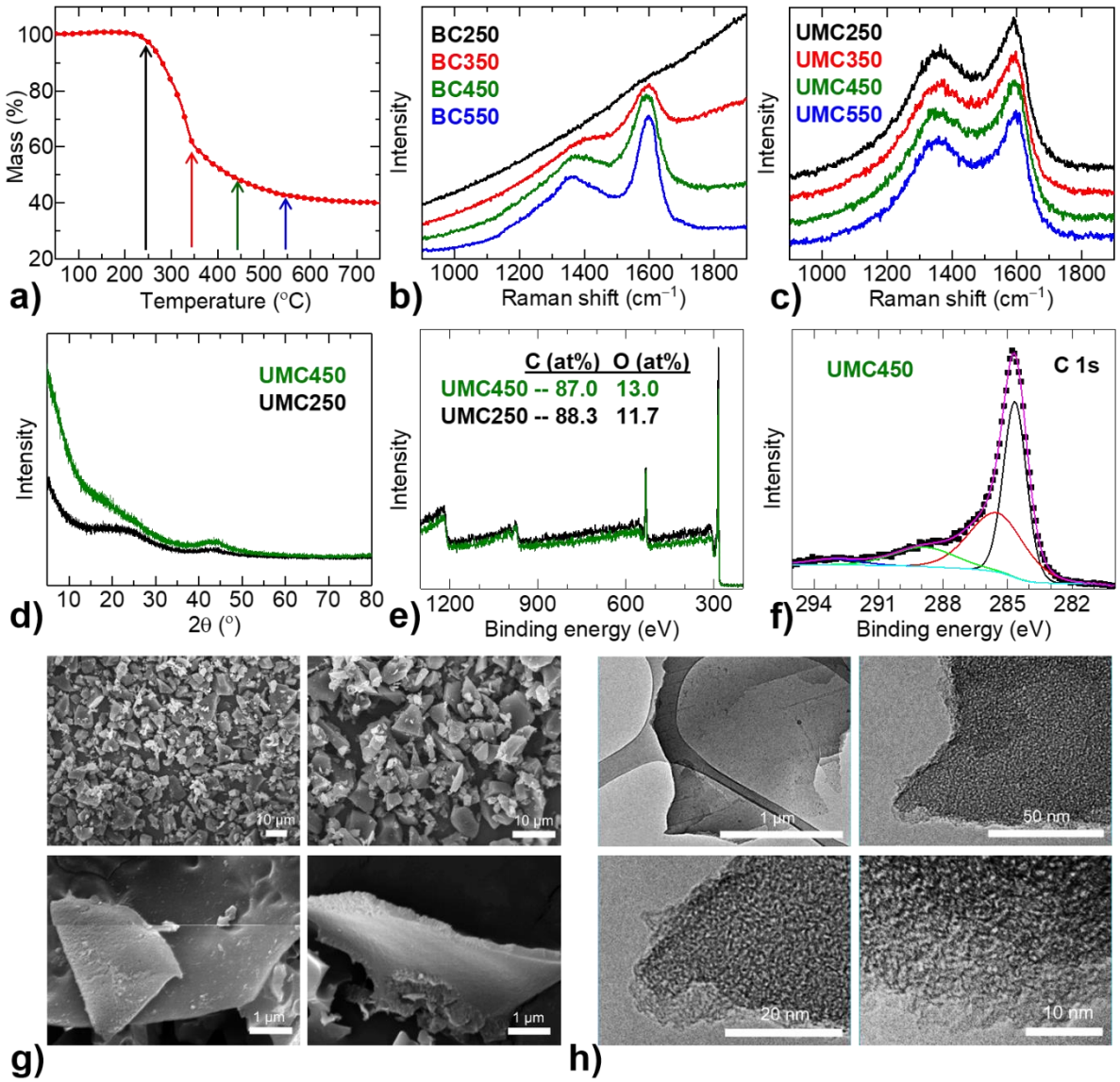

Figure 1. Characteristics of UMCs: a) Thermogravimetric curve of the pine-cones for determining the temperature of chars conversion. **b,c)** Raman spectra of chars and UMCs. **d)** PXRD patterns of UMCs. **e,f)** XPS elemental survey and C 1s core level spectra with deconvoluted peaks. **g,h)** SEM and TEM images of UMC450 – showing particle size of ≤10 micron and are in highly microporous nature. Refer to Figures S1 to S5 and Table S4 in Supplementary Information for more details on synthesis and analysis

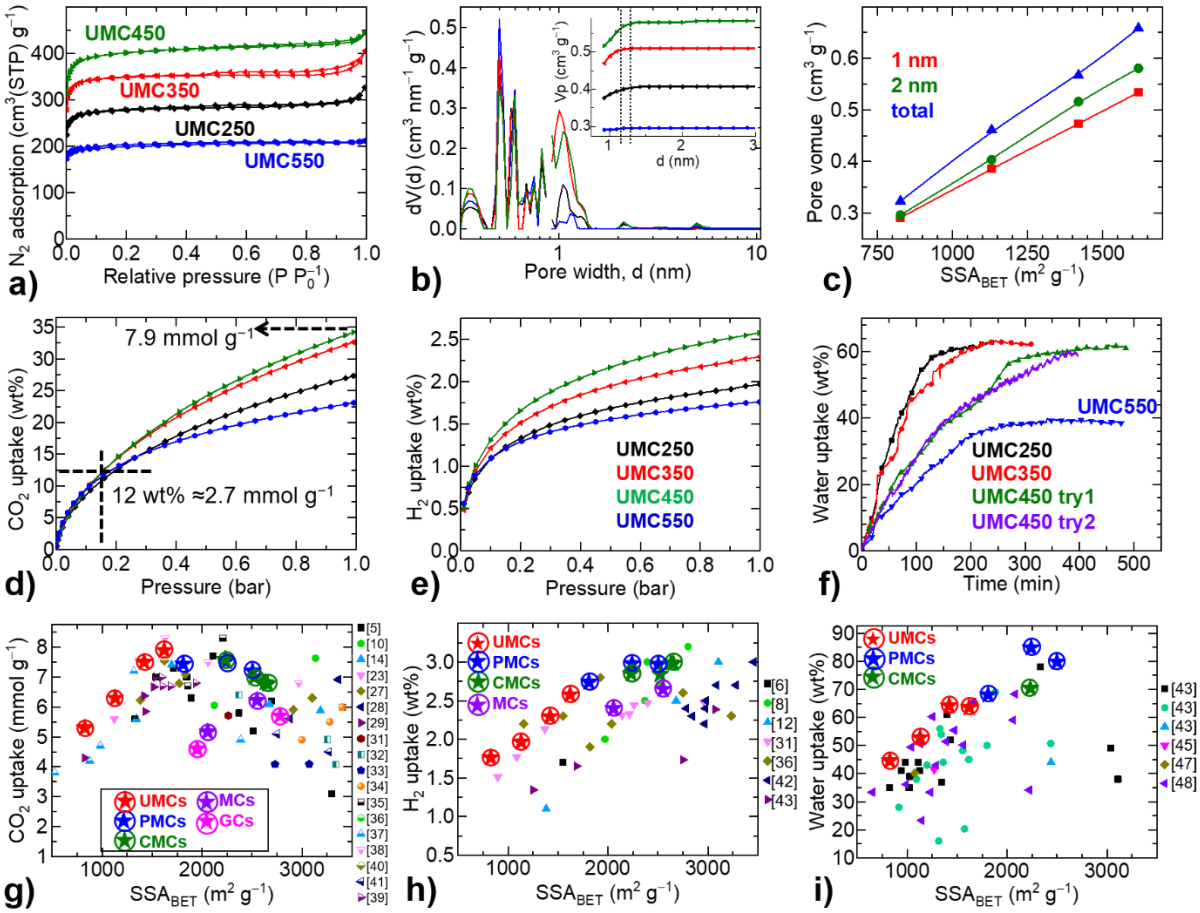

Figure 2. Porosity and adsorptive uptake characteristics: a) N_2 adsorption isotherms, at 77 K. **b)** Pore-size distribution with inset for cumulative pore volume curves; the vertical dotted guide lines to indicate the porosity development at ≤1.0 nm pore-widths. **c)** Variation of pore volumes, at 1.0 nm (ultra-microporous), 2 nm (microporous) and total (by N_2 adsorption saturation), against SSA_{BET}. **d,e)** CO_2 and H_2 uptake isotherms measured at 273 K and 77 K. **f)** H_2O vapour uptake kinetics measured at 298 K. The UMC450-try2 represent the uptake after several adsorption-desorption tests. Same colour applies for the data in a), b) d) and e). **g,h,i)** Uptake capacities of CO_2, H_2 and H_2O against SSA_{BET} of NPCs (UMCs, PMCs, CMCs, GCs and MCs) in this work and other high surface area samples from the literature deduced at relevant experimental conditions; under atmospheric pressure and at 273 K, 77 K and 298 K, respectively for CO_2, H_2 and H_2O. The data with circled star symbols represent the capacities in this study: red = UMCs, blue = PMCs, dark green/olive = CMCs, violet = MCs, magenta = GCs. Refer to **Tables 1, Figure 4,** and Figures S6,S7 and Table S3 in Supplementary Information for further details on the porosity and corresponding adsorptive uptakes.

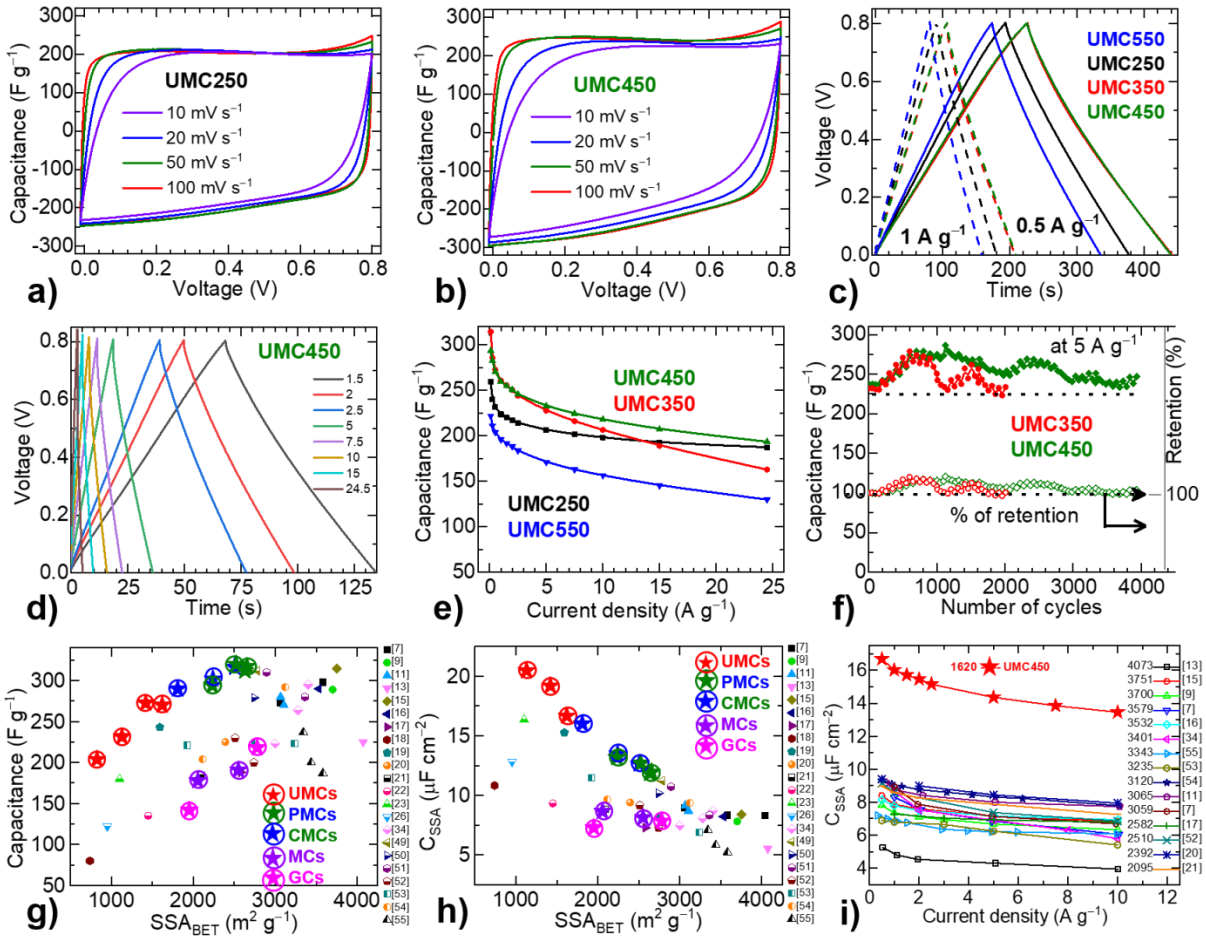

Figure 3. Supercapacitor performance in aqueous electrolyte: a,b) CV curves of UMC250 and UMC450 at different scan rates. **c)** GCD curves of UMCs at current loads of 0.5 and 1.0 A g^{-1}. **d)** GCD curves of UMC450 at higher current loads between 1.5 and 25 A g^{-1}. **e)** Specific gravimetric EDLC capacities at different current densities - rate capacitance curves. **f)** The cyclic stability data tested at 5 A g^{-1} for both UMC350 and UMC450 samples. It shows 100% capacity retention even after 4000 cycles of operation. The variation in the capacity is related to the fluctuations in room temperature, 15-35 °C, between day and night times. **g,h)** Variation of EDLC and surface area normalised EDLC capacity at 0.5 A g^{-1} against SSA_{BET} of NPCs (UMCs, PMCs, CMCs, GCs and MCs) in this work and other literature samples. The data with circled star symbols represent the capacities in this study: red = UMCs, blue = PMCs, dark green/olive = CMCs, violet = MCs, magenta = GCs. **i)** Comparative rate capacity performance curves of UMC450 and literature carbon samples of high SSA_{BET}. The literature values presented in g), h), i) are at a current density of 0.5 A g^{-1} or 1.0 A g^{-1}, in mostly from a two-electrode system. For convenience the represented data and related reference works are identified in parenthesis, where the associated surface area of each sample is also noted. All the supercapacitor data presented in this figure is for aqueous electrolyte system. See **Tables 1, Figures 4 and 5,** and Figures S8 and S9 and Tables S1 and S3 in Supplementary Information for additional details.

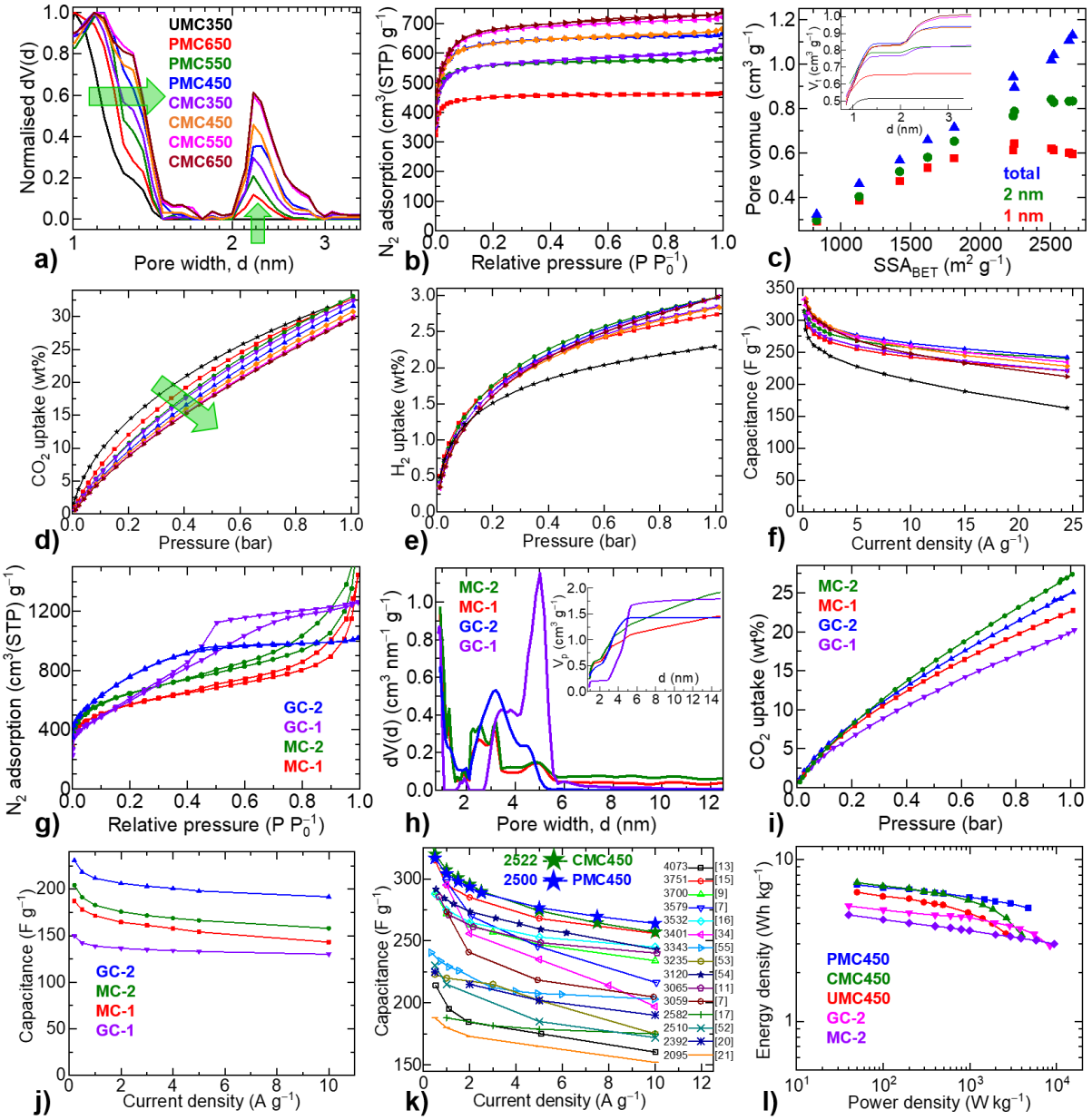

Figure 4. Control over porosity and energy storage characteristics of NPCs - Plots a) to f), and g) to j) respectively represent PMCs/CMCs and GCs/MCs: a) Pore-size distribution curves with systematically increased pore-widths. **b)** N_2 adsorption isotherms. **c)** Variation of pore volumes (at 1.0 nm, 2.0 nm, and total) against SSA_{BET} with inset for cumulative pore volume. **d,e)** CO_2 and H_2 uptake isotherms. **f)** Specific gravimetric EDLC capacities at different current densities. Same colour applies for the data in a) to f). **g)** N_2 adsorption isotherms. **h)** Pore-size distribution curves with inset for cumulative pore volume. **i)** CO_2 uptake isotherms. **j)** Specific gravimetric EDLC capacities at different current densities. **k)** Comparative rate capacity performance curves of PMCs and CMCs with respect to the literature carbon samples of high SSA_{BET}. For convenience the represented data and related reference works are identified in parenthesis, where the associated surface area of each sample is also noted. **l)** Ragone plots for the energy density variation against power density. All the supercapacitor data presented in this figure is for aqueous electrolyte system. See **Table 1, Figure 3** and Figure S9 in Supplementary Information for additional details.

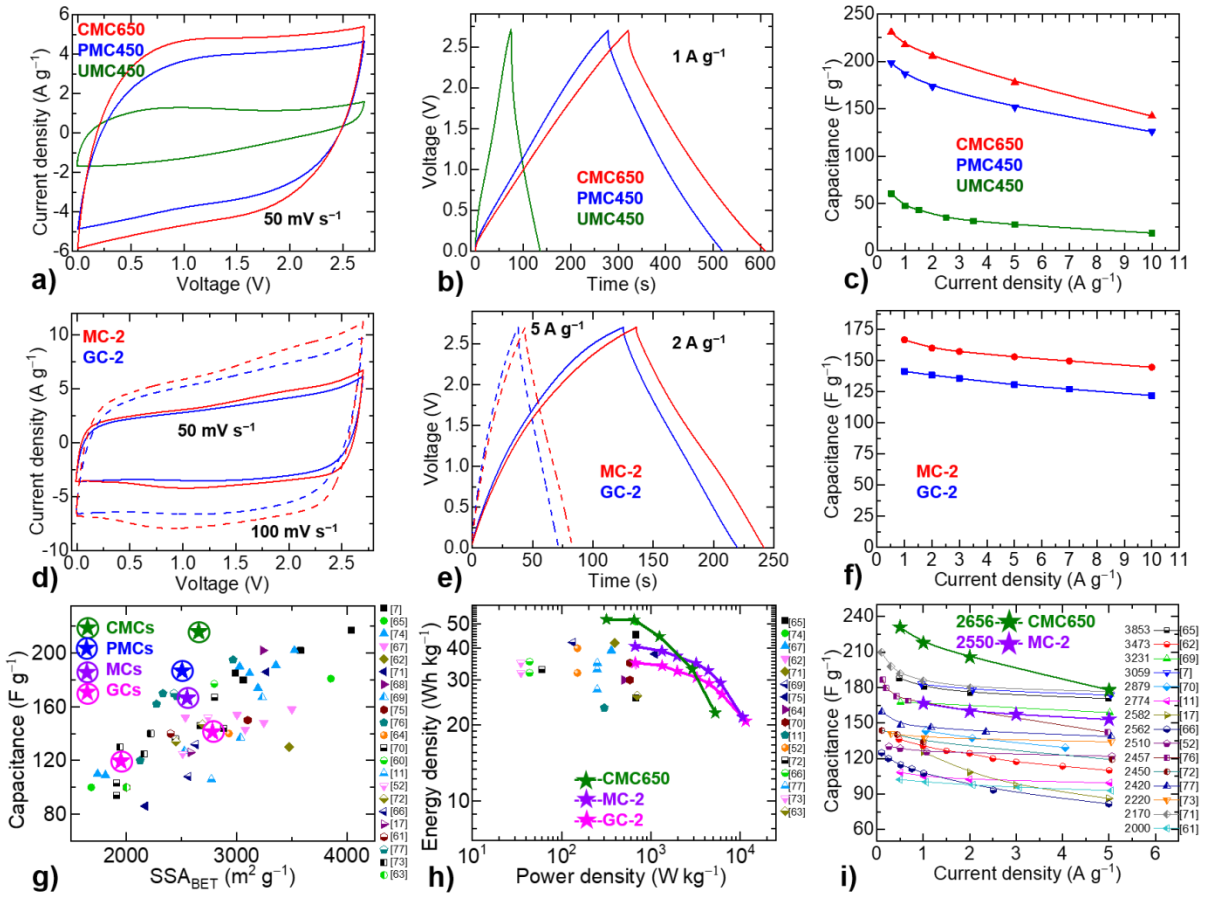

Figure 5. High voltage supercapacitor energy storage characteristics of NPCs in organic electrolyte: a,d) CV curves at 50 and 100 mV s^{-1}. **b,e)** GCD curves at 1.0, 2.0 and 5.0 A g^{-1}. **c,f)** Specific gravimetric EDLC capacities at different current densities. **g)** Variation of EDLC capacity at 1.0 A g^{-1} against SSA_{BET} of NPCs (UMCs, PMCs, CMCs, GCs and MCs) in this work, and other literature samples with reference is noted. The data with circled star symbols represent the capacities in this study: blue = PMCs, dark green/olive = CMCs, violet = MCs, magenta = GCs. **h)** Ragone plots of NPCs (PMCs, CMCs, GCs and MCs) in this work and literature carbons for the energy density against power density. **i)** Comparative rate capacity performance curves of CMCs and MCs with respect to the literature samples of high SSA_{BET}. For convenience the represented data and related reference works are identified in parenthesis, where the associated surface area of each sample is also noted. See **Tables 1,** and Table S2 and Figure S10 in Supplementary Information for additional details.

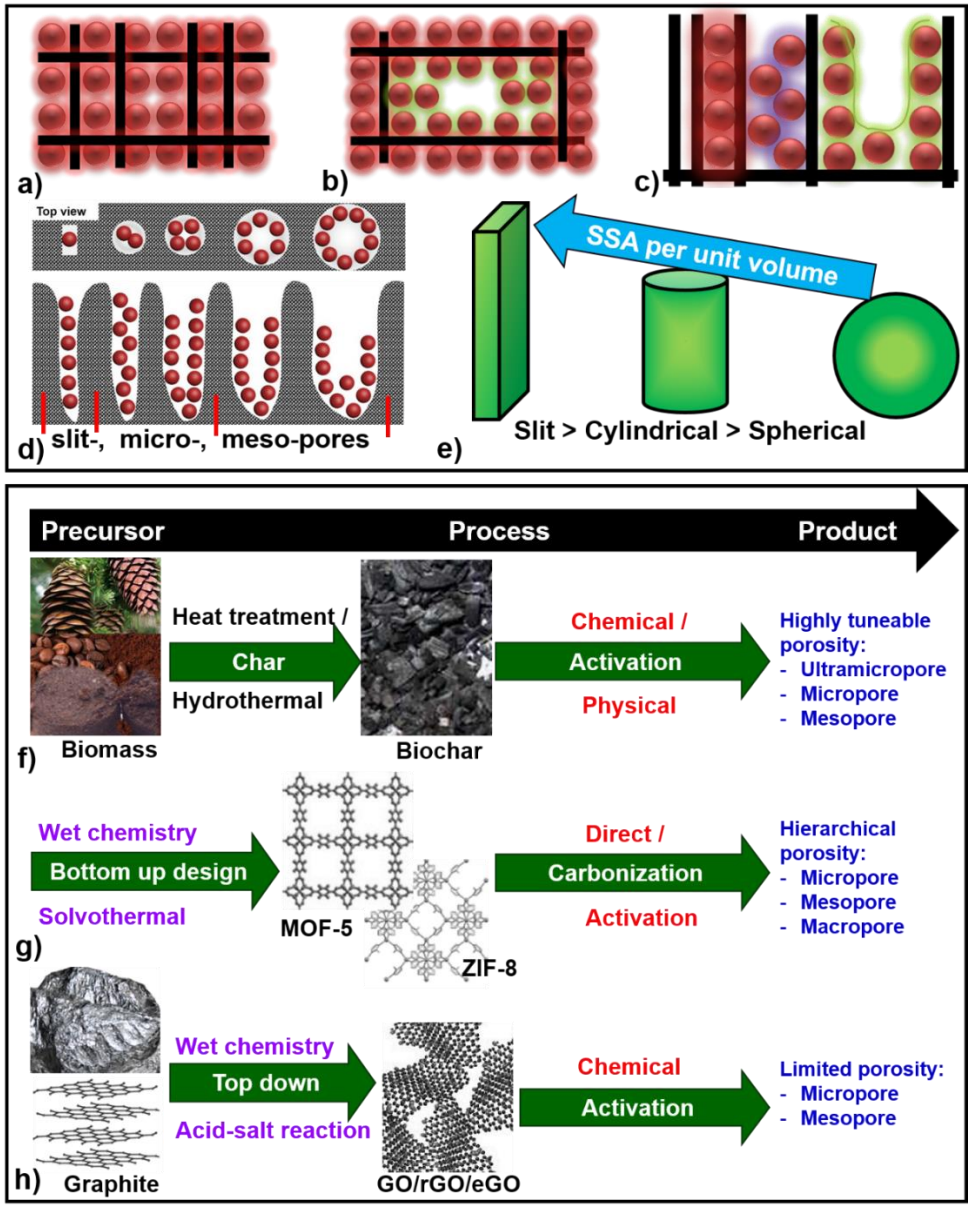

Figure 6. Porosity/pore-structure guided adsorption mechanism and synthesis of NPCs from various precursor materials: a,b,c,d) Pore occupancy or pore filling nature of molecules/ions (adsorbed density) in the various pore sizes, represented with different dimensional grills in (a, b) and surface adsorption in deep wells in (c); also depicted in top-down and cross sectional view in (d). **e)** Commonly observed pore types in NPCs and their influence on adsorption capacity – per unit pore volume basis the slit-pores offer relatively more surface area than cylindrical and spherical pores (the sphere exhibits the lowest surface area to volume ratio). Thus due to the more surface and narrow pore-widths in slit-pores the molecules experience overlapping dispersion potentials to enhance the adsorption density than large pore-widths and cylindrical or spherical pores, developed in template synthesis routes or high concentrated porogenes, due to the primarily reduced surface per unit pore volume and also the specific pore-types. **f,g,h)** Development of NPCs and expected porosities from various precursor materials including, biomass pine-cones, coffee-grounds, and predesigned 3D MOFs and 2D layered GO. The initial molecular bottom-up and top-down processing under wet chemical routes is also detailed to achieve MOFs and GO structures

Table 1: Porosity parameters; BET specific surface area (in $m^2\ g^{-1}$) and total pore volume (in $cm^3\ g^{-1}$). The QSDFT calculated microporosity at different pore-widths of 1.0 nm, 2 nm and 10 nm, and percentage of the porosity under 1.0 nm size pores from total porosity at 10 nm are summarised. The corresponding CO_2 (in mmol g^{-1}, at 273 K), H_2 (in wt%, at 77 K) H_2O (in wt%, at 298 K) uptake capacities at atmospheric pressure, and aqueous and organic EDLC capacities (in F g^{-1}) at 0.5 and 1.0 A g^{-1}, are also given.

Sample	SSA	V_t	Specific porosity from QSDFT				CO_2	H_2	H_2O	EDLC (KOH)	EDLC ($TEABF_4$)
			1.0 nm	2.0 nm	10.0 nm	% pore at 1 nm					
UMC250	1130	0.461	0.386	0.404	0.407	95.0	6.3	2.0	53.0	232	-
UMC350	1420	0.567	0.473	0.516	0.516	92.0	7.5	2.3	64.0	273	-
UMC450	1620	0.658	0.534	0.581	0.589	91.0	7.9	2.6	63.0	270	50
UMC550	826	0.323	0.291	0.296	0.299	97.0	5.3	1.8	45.0	204	-
PMC650	1810	0.715	0.577	0.653	0.664	87	7.5	2.7	68.0	290	-
PMC550	2240	0.896	0.642	0.788	0.821	78	7.5	3.0	85.0	302	-
PMC450	2504	1.018	0.621	0.842	0.945	66	7.2	3.0	80.0	317	187
CMC350	2232	0.943	0.613	0.767	0.829	74	7.6	2.9	70.0	294	-
CMC450	2522	1.042	0.613	0.828	0.936	66	7.0	2.8		320	-
CMC550	2631	1.108	0.601	0.833	1.001	60	6.8	3.0	-	312	-
CMC650	2656	1.131	0.596	0.834	1.013	59	6.8	3.0	-	317	216
MC-1	2055	2.236	0.397	0.582	1.300	30	5.2	2.4	-	178	-
MC-2	2550	2.611	0.399	0.626	1.650	24	6.2	2.7	-	191	167
GC-1	1950	1.956	0.191	0.213	1.800	11	4.6	-	-	142	-
GC-2	2780	1.578	0.342	0.516	1.450	24	5.7	-	-	218	141

Supplementary Information

Table S1. Literature reported specific gravimetric EDLC (in F g^{-1}) and surface area normalised EDLC (in µF cm^{-2}) with the corresponding BET specific surface area (in m^2 g^{-1}) values collected from wide range of porous carbons.

Reference data in the main text					
S. No.	**Sample type**	**SSA**	**C**	**C_{SSA}**	**Refs.**
1	Biomass-Algae derived AC	4037 3579 3059	335 298 273	8.3 8.3 8.9	[7]
2	Biomass-Cellulose derived AC	3700	289	7.8	[9]
3	Biomass-Gelatin-derived AC	3065 3106	280 270	9.1 8.7	[11]
4	Polymeric derived AC	4073	225	5.5	[13]
5	PANI based AC	3751	315	8.4	[15]
6	Chitosan derived AC	3532	290	8.2	[16]
7	Graphene-oxide derived carbon	2582	188	7.3	[17]
8	Polymeric-ultramicroporous carbon	1312 1243	215 175	16.4 14.1	[18]
9	Polymeric ultramicroporous carbon spheres	1692 1128	312 141	18.4 12.5	[19]
10	MgO template CVD carbon	2392	225	9.4	[20]
11	Hollow carbon spheres	2095	187	8.9	[21]
12	Polymeric-ultramicroporous carbon	1012 1001	175 165	17.3 16.5	[22]
13	MOF-derived carbon	1100	180	16.4	[23]
14	CDCs	952	122	12.8	[26]
15	Biomass-Chestnut derived carbon	3401 3277 3138 2998	295 264 215 223	8.7 8.1 6.9 7.4	[34]
16	Biomass-cellulose AC	2781	312	11.2	[49]
17	Urea-cellulose- AC	2743	279	10.2	[50]
18	Peanut dregs AC	3361 2893	280 310	8.3 10.7	[51]
19	Tannic acid derived AC	2740 2510	200 230	7.3 9.2	[52]
20	Lignin derived AC	3235 2750 1924	223 223 221	6.9 8.1 11.5	[53]
21	Biomass-Ricehusk derived carbon	3120 2113	292 204	9.4 9.7	[54]
22	Asphalt derived AC	3581 3438	187 200	5.2 5.8	[55]

		3343	237	7.1	

Additional data references

S. No.	Sample type	SSA	C	C_{SSA}	Refs.
23	Asphalt derived AC	2407 2000 1424	190 170 145	7.9 8.5 10.2	S[78]
24	Peachgum AC	1535 1279 1256	257 203 190	16.7 15.9 15.1	S[79]
25	Glucose-cellulose AC	1516	249	16.4	S[80]
26	Glucose-CNT AC	2021 1718 1390 1310	218 220 117 121	10.8 12.8 8.4 9.2	S[81]
27	Soybean dregs AC	2090 2000 1131	220 308 205	10.5 15.4 18.1	S[82]
28	Pyrolysis of lignin	1307 1269 1084	200 225 173	15.3 17.7 16.0	S[83]
29	Silica-template AC	1920 1865	150 130	7.8 7.0	S[84]
30	PANI-based AC	2439	267	10.9	S[85]
31	MgO template polymer derived AC	2733	190	7.0	S[86]
32	Anthracite derived AC	2357 2307 2075 1959	230 270 270 200	9.8 11.7 13.0 10.2	S[87]
32	Zeolite template CVD carbon	710 2950 1520	145 260 125	20.4 8.8 8.2	S[88]
33	Biomass-Lignin-derived carbon	1750 2136 1970 2120 1912 1585	171 195 183 206 160 145	9.8 9.1 9.3 9.7 8.4 9.2	S[89]
34	Biomass-Starch derived carbon	1150 1521 1681 1348 1845 2200 2311	137 171 165 158 202 229 202	11.9 11.2 9.8 11.7 11.0 10.4 8.7	S[90]
35	Macroalgae AC	1979 1528	185 200	9.3 13.1	S[91]

		952	180	18.9	
36	Biomass-Jujun grass derived carbon	2800 1893	220 253	7.9 13.4	S[92]
	Biomass--carrageenan	2502	261	10.4	--
	Biomass--wood	2294	225	9.8	--
37	Biomass-Sugarcane derived carbon	2341	226	9.7	S[93]
38	Biomass-Cornstraw derived carbon	3237	229	7.1	S[94]
	YP50	1493	127	8.5	--
	Biomass-Corngrains	3199	257	8.0	--
	Biomass-Corncob	3054	328	10.7	--
	Biomass-Cornstover	1671	236	14.1	--
39	Biomass-Papaya derived carbon	3643	234	6.4	S[95]
40	Coal derived carbon	2574	263	10.2	S[96]
		2790	318	11.4	--
		3261	337	1.03	--
		3347	344	10.3	--
		3223	340	10.6	--
		2659	232	8.7	--
41	Biomass-Algae derived carbon	2825	315	11.2	S[97]
42	Corn leaf AC	2507	215	8.6	S[98]
		2002	178	8.9	
		1878	140	7.6	
		1835	165	9.0	
		1680	128	7.6	
		1417	148	10.4	
43	Silica-template mesocarbon	2545	274	10.8	S[99]
		1205	132	11.0	
44	Silica-template OMC	1492	160	10.7	S[100]
45	Glucose AC	1510	205	13.6	S[101]
		1440	190	13.2	
		1175	195	16.6	
46	Cellulose AC	2300	260	11.3	S[102]
		2220	210	9.5	
47	Aerogels	2119	235	11.1	S[103]
		1589	175	11.0	
48	MgO template CVD carbon capsules	2053	210	10.2	S[104]
		1854	217	11.7	
		1633	217	13.3	
49	Cellulose AC	3404	273	8.0	S[105]

Table S2. Literature reported specific gravimetric EDLC (in F g^{-1}), measured in 1 M tetraethylammonium tetrafluoroborate ($TEABF_4$)/acetonitrile (AN) electrolyte, at 1.0 A g^{-1}, with the corresponding BET specific surface area (in m^2 g^{-1}) and pore volume (in cm^3 g^{-1}) values collected from wide range of porous carbons. The energy density at a particular power density is also noted with relevant reference works.

Reference data in the main text							
S. No.	**Sample type**	**SSA**	**Vp**	**C**	**E**	**P**	**Refs.**
1	HPSCA – S-doped mesoporous carbon aerogel	4037 3579 3059 2988	2.62 2.40 1.51 1.75	217 202 180 185	-	-	[7]
2	ACs from pentaerythritol melamine phosphate, HPGCS-600 YP-50	3853 1681	2.79 0.79	181 100	45.3 25.5	675 675	[65]
3	Mesoporous ACs from sucrose, phenol, formaldehyde with graphene-oxide, PF16G-HA SU24G-HA PVA20G-HA LI24G-HA CE24G-HA G-HA RP20	3523 3355 3192 3026 3117 1810 1739	2.13 2.03 1.70 2.40 1.44 0.90 0.64	202 191 174 190 185 116 110	51	674	[74]
4	ACs from asphalt with graphene-oxide	3500 3246 3077 3003 2535		158 148 143 154 152	39.2	360	[67]
5	Mesoporous carbons from pitch-based polymers foam	3473	1.71	130	34.5	679	[62]
6	ACs from seaweed	3270 2170	1.94 1.02	186 86	42.0	390	[71]
7	AC-KOH – biomass waste	3237		202	-	-	[68]
8	ACs from self-silica template polymer	3231 3035 2526		167 137 127	42.2	134	[69]
9	Activated carbon from microwaved graphene-oxide	3100		150	38.0	1100	[75]
10	ACs from various	1500		120-	20-40	-	[59]

	precursors	- 3000		180			
11	ACs from biowaste	2967 2457 2331 2273 2125	1.35 1.08 1.03 1.01 0.98	195 168 170 162 120	-	-	[76]
12	N-(4.6at%)doped AC from Samanea	2930	1.37	≈140	30.0	500	[64]
13	ACs from raw hemp stem	2879 2801 2671 2446 1909 1910	1.16 1.71 1.76 1.06 0.86 0.72	144 167 146 136 103 94	35.0 30.0	580 580	[70]
14	AC from Soybean	2797 1197	2.48 0.68	177 100	-	-	[60]
15	AC from confined gelatin (PCNS-G-4)	2774		106	23.3 10.3	300 18.4k	[11]
	AC from tannic acid (CK-900 CK-800)	2740 2510		152 125	40.0 32.0	150 150	[52]
16	AC from Silica template pyrrole	2690 2450	1.26 1.17	147 134	33.0	60.0	[72]
17	ACs from graphite oxide and coal tar pitch	2626 2562	1.80 2.34	132 108	35.4 32.0	43.7 43.7	[66]
18	AC from graphene-oxide (aPG-10)	2582		126	-	-	[17]
	ACs from range of precursors	1500 - 2500		100-190	-	-	[58]
19							
20	Commercially available ACs – six samples	2000 - 2400	1.3-1.5	100-140	-	-	[61]
21	CDCs from Silica templates	2430 2420 2250		128 148 160	27.5 33.0 35.0	250 250 250	[77]
22	ACs from potassium citrate	1940 2220 2160	0.96 1.11 1.30	130 140 125	- 35.0 32.0	- 35.0 35.0	[73]
23	AC from pyrrole	2000	1.00	100	26.0	700	[63]
Additional data references							
24	Silica template mesoporous activated	1900		100	-	-	S[84]

	carbon						
25	B, N-doped AC from sisal	2017	1.33	116	24.3	613	S[106]
26	AC from clews of polymers nanobelts	2291	1.29	102	29.8	345	S[107]
27	ACs	2347 1681	1.15 0.78	100 90	-	-	S[108]
28	Carbon aerogel microspheres from polymers	1450	0.75	100	26.8	34.0	S[109]
29	AC from cotton waste	1550	0.69	112	29.5	310	S[110]
30	CDCs – carbide derived carbons	1000 - 1600		100-140	-	-	S[111]

Table S3: Literature reported CO_2 adsorption capacities (in mmol g^{-1}, measured at 273 K and 1 bar) and the BET specific surface area (in m^2 g^{-1}) values collected from wide range of porous solids.

Reference data in the main text				
S. No.	**Precursor/sample type**	**SSA_{BET}**	**CO_2 uptake**	**Ref.**
1	Pine Cone	2110	7.7	[5]
	Coconut shell	1535	7.0	
	Coconut shell	1327	5.6	
	Black Locust	2511	7.2	
	Empty fruit bench	2510	5.2	
	Peanut shell	1713	7.3	
	Rice husk	2695	6.2	
	African palm shell	1890	6.3	
	Bamboo	1846	7.0	
	Celtuce leaves	3404	6.0	
	Cellulose	2370	5.8	
	Arundo donax	3298	3.1	
2	PAC-500/2	1486	4.8	[10]
	PAC-550/2	2122	6.1	
	PAC-600/2	2526	7.0	
	PAC-650/2	3135	7.6	
	PAC-700/2	3529	7.7	
	PAC-750/2	3759	7.3	
	PAC-800/2	3931	7.1	
	PAC-500/4	1772	3.9	
3	PANI_C400_K615	3185	5.9	[14]
	PANI_C400_KC650	1695	7.41	

	PANI_C400_KC800	2675	6.09	
	PANI_C550_K800	4240	4.31	
4	ZIF-8 carbon	1120	5.6	[23]
5	CDCs	1383	6.23	[27]
		1832	7.09	
		1772	6.79	
	activated micro-TiC-CDC	2911	5.91	
		3101	6.31	
		2565	6.92	
		2229	6.18	
6	CEM700	2878	5.61	[28]
	CEM750	3360	6.92	
	CEMFAET	3698	5.90	
7	Polyurethene foam-ultramicroporous N-doped carbons	1470 1430 1077 826 1516 1420	4.36 5.85 3.67 4.29 6.67 6.37	[29]
8	porous nitrogen doped carbon	2141	5.85	[31]
		2215	5.13	
		2261	5.71	
		2960	5.45	
		2397	5.63	
		2141	5.85	
		2215	5.13	
9	ACDS-500-2	2112	5.98	[32]
	ACDS-500-4	3255	4.91	
	ACDS-500-6	3337	4.07	
	ACDS-800-4	2367	6.40	
	ACDS-800-6	2844	5.60	
10	SR-KOH	3072	4.09	[33]
	SS-KOH	2730	4.08	
	SS-1000	654	4.52	
11	ANCs-3-600	2998	4.90	[34]
	ANCs-3-650	3277	5.50	
	ANCs-3-700	3401	6.00	
	ANCs-3-800	3138	4.60	
12	NPC-500	1854	6.70	[35]
	NPC-600	2208	8.30	
	NPC-700	2565	7.20	
13	LAC2600	1157	4.40	[36]
	LAC2700	1551	7.40	
	LAC2800	1924	6.50	
14	Organic-inorganic-ultramicroporous N-doped carbons	1317 1342 2386 982	7.2 5.6 4.9 4.7	[37]

		875 526	4.2 3.8	
15	BILP-5	626	2.90	[38]
	CPC-550	1630	8.30	
	CPC-600	2059	7.50	
	CPC-650	2967	6.80	
	CPC-700	3242	5.90	
	CPC-800	2872	5.40	
16	Coconut shell+urea-derived N-doped carbons	1535 1596 1604 1687 1937	7.0 7.0 6.7 6.7 6.8	[39]
17	CG 400 2-1	2073	7.17	[40]
	CG 400 4-1	2785	5.09	
	CG 700 2-1	1624	7.55	
	CG 700 4-1	2620	6.89	
18	MOF-derived carbon	2747	5.10	[41]
		3268	4.50	
		1510	5.54	
		1455	5.56	
		2462	4.53	
		1900	5.05	

Additional data references

S. No.	**Precursor/sample type**	**SSA_{BET}**	**CO_2 uptake**	**Ref.**
19	a-CL	3404	6.04	S[105]
20	PC-1-1	1898	3.81	S[112]
	PC-1-2	1790	4.40	
	PC-1-3	2424	4.10	
	PC-2-2	2358	4.77	
	PC-2-3	1829	5.03	
	PC-2-4	1684	4.62	
21	LSB1-800	1614	6.90	S[113]
	LSB2-800	2046	6.30	
	LSB3-800	2230	6.80	
	LSB4-800	1717	4.60	
22	THPS-C	3125	5.12	S[114]
23	C-HPS	358	4.38	S[115]
	C-PPy@HPS-10	408	4.74	
	C-PPy@HPS-20	444	4.89	
	C-PPy@HPS-30	386	4.81	

	A-HPS	2001	5.18	
	A-PPy@HPS-10	1930	5.41	
	A-PPy@HPS-20	2080	5.80	
	A-PPy@HPS-30	1749	5.48	
	A-PPy@PS-80	929	2.73	
24	biomass-starch-derived carbon	1035	3.40	S[116]
		2549	5.02	
		2543	5.75	
25	petroleum coke- derived carbon	915	4.56	S[117]
		1433	6.08	
		1586	6.08	
		2433	6.12	
		538	3.80	
		1600	4.89	
26	petroleum coke-derived carbon	756	4.38	S[118]
		856	4.54	
		1394	5.12	
		1666	5.93	
		2273	5.61	
		2419	5.20	
		2136	4.84	
		3125	4.91	
		3259	4.49	
27	polymeric-derived carbon	1699	2.68	S[119]
		1532	3.04	
		1339	3.35	
		1227	3.48	
28	OTS-1-550	741	4.13	S[120]
	OTS-1-650	1377	6.15	
	OTS-1-750	2676	4.52	
29	MOF-derived carbon	682	3.52	S[121]
		823	4.05	
		1115	4.62	
		1241	4.52	
		1129	4.75	
		1059	4.62	
		959	4.41	
		909	4.17	
30	pine cone-derived carbon	1680	7.8	S[122]
		2110	7.8	

		1650	6.9	
		1640	7.4	
		1260	6.2	
31	NHC-600-1	1037	5.15	S[123]
	NHC-600-2	1187	5.73	
	NHC-600-3	1970	6.32	
	NHC-600-4	2339	5.93	
	NHC-650-1	1593	6.53	
	NHC-650-2	1694	6.28	
	NHC-650-3	1952	6.40	
	NHC-650-4	2492	6.00	
	NHC-700-1	2234	6.79	
	NHC-700-2	2241	6.67	
	NHC-700-3	2782	6.54	
	NHC-700-4	2995	5.68	
	NC-650-1	1483	6.15	
32	polymeric-derived carbon	519	2.01	S[124]
		1008	4.59	
		1463	5.17	
		1917	6.31	
		2782	5.55	
		3180	4.8	
		3158	4.71	
		3325	4.33	
		867	3.63	
		1017	4.61	
		1217	3.88	
		1020	5.03	
33	NC-600-1	879	4.77	S[125]
	NC-600-2	1135	5.41	
	NC-600-3	1850	6.30	
	NC-600-4	1562	6.11	
	NC-650-1	1483	6.15	
	NC-650-2	1487	6.28	
	NC-650-3	2322	6.26	
	NC-650-4	2521	6.19	
	NC-700-1	1349	6.52	
	NC-700-2	1967	6.46	
	NC-700-3	2690	6.44	
	NC-700-4	2599	5.63	
	C-650-1	832	5.01	
34	PAF-1	5300	2.05	S[126]
	PAF-derived carbon	1064	3.20	

		1568	4.08	
		2325	7.19	
		2434	5.85	
		2568	5.78	
		2926	5.38	
		2857	5.22	
		1748	4.04	
35	CP-4–600	2050	4.00	S[127]
	CP-4–650	3260	4.40	
	CP-4–700	3480	4.10	
	CP-4–800	3450	4.10	
	CP-4–850	3360	4.30	
	CP-2–600	1700	6.20	
	CP-2–650	2520	5.90	
	CP-2–700	2940	5.90	
	CP-2–800	3410	4.30	

Supplementary references

[78] P. Liu, Z. Si, W. Lv, X. Wu, R. Ran, D. Weng, F. Kang, Synthesizing multilayer graphene from amorphous activated carbon via ammonia-assisted hydrothermal method, **Carbon, 2019, 152, 24-32**.

[79] Y. Lin, Z. Chen, C. Yu, W. Zhong, Heteroatom-doped sheet-like and hierarchical porous carbon based on natural biomass small molecule peach gum for high-performance supercapacitors, **ACS Sustainable Chem. Eng., 2019, 7, 3389-3403**.

[80] X. Zhang, H. Li, B. Qin, Q. Wang, X. Xing, D. Yang, L. Jin, Q. Cao, Direct synthesis of porous graphitic carbon sheets grafted on carbon fibers for high-performance supercapacitors, **J. Mater. Chem. A, 2019, 7, 3298-3306**.

[81] N. Rey-Raap, M. Enterría, J. I. Martins, M. F. R. Pereira, J. L. Figueiredo, Influence of multiwalled carbon nanotubes as additives in biomass-derived carbons for supercapacitor applications, **ACS Appl. Mater. Interf., 2019, 11, 6066-6077**.

[82] Z. Li, H. Mi, Z. Bai, C. Ji, L. Sun, S. Gao, J. Qiu, Sustainable biowaste strategy to fabricate dual-doped carbon frameworks with remarkable performance for flexible solid-state supercapacitors, **J. Power Sour., 2019, 418, 112-121**.

[83] F. Liu, Z. Wang, H. Zhang, L. Jin, X. Chu, B. Gu, H. Huang, W. Yang, Nitrogen, oxygen and sulfur co-doped hierarchical porous carbons toward high-performance supercapacitors by direct pyrolysis of kraft lignin, **Carbon, 2019, 149, 105-116**.

[84] J.-G. Li, Y.-F. Ho, M. M. M. Ahmed, H.-C. Liang, S.-W. Kuo, Mesoporous carbons templated by PEO-PCL block copolymers as electrode materials for supercapacitors, **Chem. Eur. J. 2019, 25, 10456-10463**.

[85] Z. Dai, P.-G. Ren, Y.-L. Jin, H. Zhang, F. Ren, Q. Zhang, Nitrogen-sulphur Co-doped graphenes modified electrospun lignin/ polyacrylonitrile-based carbon nanofiber as high performance supercapacitor, **J. Power Sour., 2019, 437, 226937**.

[86] Y. Wen, L. Zhang, J. Liu, X. Wen, X. Chen, J. Ma, T. Tang, E. Mijowska, Hierarchical porous carbon sheets derived on a MgO template for high-performance supercapacitor applications, **Nanotechnology, 2019, 30, 295703**.

[87] J. Qi, B. Jin, P. Bai, W. Zhang, L. Xu, Template-free preparation of anthracite-based nitrogen-doped porous carbons for highperformance supercapacitors and efficient electrocatalysts for the oxygen reduction reaction, **RSC Adv., 2019, 9, 24344-24356**.

[88] T. Lee, S. H. Ko, S. J. Cho, R. Ryoo, Ultramicroporous carbon synthesis using lithium-ion effect in ZSM-5 zeolite template, **Chem. Mater., 2018, 30, 6513-6520**.

[89] H. C. Ho, N. A. Nguyen, K. M. Meek, D. M. Alonso, S. H. Hakim, A. K. Naskar, A solvent-free synthesis of lignin-derived renewable carbon with tunable porosity for supercapacitor electrodes, **ChemSusChem, 2018, 11, 2953-2959**.

[90] J. Cao, C. Zhu, Y. Aoki, H. Habazaki, Starch-derived hierarchical porous carbon with controlled porosity for high performance supercapacitors, **ACS Sustainable Chem. Eng., 2018, 6, 7292-7303**.

[91] M. Ren, Z. Jia, Z. Tian, D. Lopez, J. Cai, A. B. Jorge, M.-M. Titirici, High performance N-doped carbon electrodes obtained *via* hydrothermal carbonization of macroalgae for supercapacitor applications, **ChemElectroChem 2018, 5, 2686-2693**.

[92] 55. Y. Liu, B. Huang, X. Lin, Z. Xie, Biomass-derived hierarchical porous carbons: boosting the energy density of supercapacitors via an ionothermal approach, **J. Mater. Chem. A, 2017, 5, 13009-13018**.

[93] Q. Niu, K. Gao, Q. Tang, L. Wang, L. Han, H. Fang, Y. Zhang, S. Wang, L. Wang, Large-size graphene-like porous carbon nanosheets with controllable N-doped surface derived from sugarcane bagasse pith/chitosan for high performance supercapacitors, **Carbon, 2017, 123, 290-298**.

[94] Y. Lu, S. Zhang, J. Yin, C. Bai, J. Zhang, Y. Li, Y. Yang, Z. Ge, M. Zhang, L. Wei, M. Ma, Y. Ma, Y. Chen, Mesoporous activated carbon materials with ultrahigh mesopore volume and effective specific surface area for high performance supercapacitors, **Carbon, 2017, 124, 64-71**.

[95] S. Wang, R. Wang, Y. Zhang, L. Zhang, Highly porous carbon with large electrochemical ion absorption capability for high-performance supercapacitors and ion capacitors, **Nanotechnology, 2017, 28, 445406**.

[96] P. Chang, Z. Qin, Facile fabrication of hierarchical porous carbon based on extract separated from coal with outstanding electrochemical performance, **RSC Adv., 2017, 7, 33843-33850**.

[97] X. Wu, Z. Tian, L. Hu, S. Huang, J. Cai, Macroalgae-derived nitrogen-doped hierarchical porous carbons with high performance for H_2 storage and supercapacitors, **RSC Adv., 2017, 7, 32795-32805**.

[98] X. Yang, C. Li, Yue Chen, Hierarchical porous carbon with ultrahigh surface area from corn leaf for high performance supercapacitors application, **J. Phys. D: Appl. Phys., 2017, 50, 055501**.

[99] D. K. Singh, K. S. Krishna, S. Harish, S. Sampath, M. Eswaramoorthy, No more HF: Teflon- assisted ultrafast removal of silica to generate high- surface- area mesostructured carbon for enhanced CO_2 capture and supercapacitor performance, **Angew. Chem. Int. Ed., 2016, 55, 2032-2036**.

[100] A. Sanchez-Sanchez, V. Fierro, M. T. Izquierdo, A. Celzard, Functionalized, hierarchical and ordered mesoporous carbons for high-performance supercapacitors, **J. Mater. Chem. A, 2016, 4, 6140-6148**.

[101] M. Sevilla, L. Yu, C. O. Ania, M.-M. Titirici, Supercapacitive behavior of two glucose-derived microporous carbons: direct pyrolysis versus hydrothermal carbonization, **ChemElectroChem, 2014, 1, 2138-2145**.

[102] C. Falco, J. M. Sieben, N. Brun, M. Sevilla, T. van der Mauelen, E. Morallen, D. Cazorla-Amors, M.-M. Titirici, Hydrothermal carbons from hemicellulose-derived aqueous hydrolysis products as electrode materials for supercapacitors, **ChemSusChem, 2013, 6, 374-382**.
[103] D. Liu, J. Shen, N. Liu, H. Yang, A. Du, Preparation of activated carbon aerogels with hierarchically porous structures for electrical double layer capacitors, **Electrochimica Acta, 2013, 89, 571-576**.
[104] K. Xie, X. Qin, X. Wang, Y. Wang, H. Tao, Q. Wu, L. Yang, Z. Hu, Carbon nanocages as supercapacitor electrode materials, **Adv. Mater., 2012, 24, 347-352**.
[105] R. Wang, P. Wang, X. Yan, J. Lang, C. Peng, Q. Xue, Promising porous carbon derived from celtuce leaves with outstanding supercapacitance and CO_2 capture performance, **ACS Appl. Mater. Interfaces, 2012, 4, 5800-5806**.
[106] H. Wu, W. Yuan, Y. Zhao, D. Han, X. Yuan, L. Cheng, B, N-dual doped sisal-based multiscale porous carbon for high-rate supercapacitors, **RSC Adv., 2019, 9, 1476-1486.**
[107] J. Zou, W. Tu, S.-Z. Zeng, Y. Yao, Q. Zhang, H. Wu, T. Lan, S. Liu, X. Zeng, High-performance supercapacitors based on hierarchically porous carbons with a three-dimensional conductive network structure, **Dalton Trans., 2019, 48, 5271-5284.**
[108] N. Jäckel, D. Weingarth, A. Schreiber, B. Krüner, M. Zeiger, A. Tolosa, M. Aslan, V. Presser, Performance evaluation of conductive additives for activated carbon supercapacitors in organic electrolyte, **Electrochim. Acta, 2016, 191, 284-298.**
[109] F. Li, A. Ahmad, L. Xie, G. Sun, Q. Kong, F. Su, Y. Ma, Y. Chao, X. Guo, X. Wei, C.-M. Chen, Phosphorus-modified porous carbon aerogel microspheres as high volumetric energy density electrode for supercapacitor, **Electrochim. Acta, 2019, 318, 151-160.**
[110] M. Vijayakumar, R. Santhosh, J. Adduru, T. N. Rao, M. Karthik, Activated carbon fibres as high performance supercapacitor electrodes with commercial level mass loading, **Carbon, 2018, 140, 465-476.**
[111] J. Chmiola, G. Yushin, Y. Gogotsi, C. Portet, P. Simon, P. L. Taberna, Anomalous increase in carbon capacitance at pore sizes less than 1 nanometer, **Science, 2006, 313, 1760-1763.**
[112] H. Yuan, J. Chen, D. Li, H. Chen, Y. Chen, 5 Ultramicropore-rich renewable porous carbon from biomass tar with excellent adsorption capacity and selectivity for CO_2 capture, **Chem. Eng. J., 2019, 373, 171-178**.
[113] G. Singh, K. S. Lakhi, K. Ramadass, C. Sathish, A. Vinu, High-performance biomass-derived activated porous biocarbons for combined pre- and post-combustion CO_2 capture, **ACS Sustainable Chem. Eng., 2019, 7, 7412-7420**.
[114] Q.-M. Zhang, T.-L. Zhai, Z. Wang, G. Cheng, H. Ma, Q.-P. Zhang, Y.-H. Zhao, B. Tan, C. Zhang, Hyperporous carbon from triptycene-based hypercrosslinked polymer for iodine capture, **Adv. Mater. Interf., 2019, 6, 1900249**.
[115] R. Cai, B. You, M. Chen, L. Wu, Metal-free core-shell structured N-doped carbon/carbon heterojunction for efficient CO_2 capture, **Carbon, 2019, 150, 43-51**.
[116] Y.-J. Heo, S.-J. Park, H_2O_2/steam activation as an eco-friendly and efficient top-down approach to enhancing porosity on carbonaceous materials: the effect of inevitable oxygen functionalities on CO_2 capture, **Green Chem., 2018, 20, 5224-5234**.
[117] E. Jang, S. W. Choi, S.-M. Hong, S. Shin, K. B. Lee, Development of a cost-effective CO_2 adsorbent from petroleum coke via KOH activation, **Appl. Surface Sci., 2018, 429, 62-71**.

[118] L. Rao, S. Liu, J. Chen, L. Wang, L. An, P. Yang, X. Hu, Single-step synthesis of nitrogen-doped porous carbons for CO_2 capture by low-temperature sodium amide activation of petroleum coke, **Energy Fuels, 2018, 32, 12787-12794**.
[119] Z. Tian, N. Fechler, M. Oschatz, T. Heil, J. Schmidt, S. Yuan, M. Antonietti, $C_2N_xO_{1-x}$ framework carbons with defined microporosity and co-doped functional pores, **J. Mater. Chem. A, 2018, 6, 19013-19019**.
[120] Y. Zhang, P. Zhang, W. Yu, J. Wang, Q. Deng, J. Yang, Z. Zeng, M. Xu, S. Deng, Facile and controllable preparation of ultramicroporous biomass-derived carbons and application on selective adsorption of gas mixtures, **Ind. Eng. Chem. Res., 2018, 57, 14191-14201**.
[121] Y. Pan, Y. Zhao, S. Mu, Y. Wang, C. Jiang, Q. Liu, Q. Fang, M. Xue, S. Qiu, Cation exchanged MOF-derived nitrogen-doped porous carbons for CO_2 capture and supercapacitor electrode materials, **J. Mater. Chem. A, 2017, 5, 9544-9552**.
[122] B. Zhu, C. Shang, Z. Guo, Naturally nitrogen and calcium-doped nanoporous carbon from pine cone with superior CO_2 capture capacities, **ACS Sustainable Chem. Eng., 2016, 4, 1050-1057**.
[123] L. Guo, J. Yang, G. Hu, X. Hu, L. Wang, Y. Dong, H. DaCosta, M. Fan, Role of hydrogen peroxide preoxidizing on CO_2 adsorption of nitrogen-doped carbons produced from coconut shell, **ACS Sustainable Chem. Eng., 2016, 4, 2806-2813**.
[124] K. Huang, S.-H. Chai, R. T. Mayes, S. Tan, C. W. Jones, S. Dai, Significantly increasing porosity of mesoporous carbon by $NaNH_2$ activation for enhanced CO_2 adsorption, **Micropor. Mesopor. Mater., 2016, 230, 100-108**.
[125] M. Yang, L. Guo, G. Hu, X. Hu, L. Xu, J. Chen, W. Dai, M. Fan, Highly cost-effective nitrogen-doped porous coconut shell-based CO_2 sorbent synthesized by combining ammoxidation with KOH activation, **Environ. Sci. Tech., 2015, 49, 7063-7070**.
[126] Y. Li, T. Ben, B. Zhang, Y. Fu, S. Qiu, Ultrahigh gas storage both at low and high pressures in KOH-activated carbonized porous aromatic frameworks, **Sci. Rep., 2013, 3, 2420**.
[127] M. Sevilla, P. Valle- Vigón, A. B. Fuertes, N- doped polypyrrole- based porous carbons for CO_2 capture, **Adv. Funct. Mater., 2011, 21, 2781-2787**.

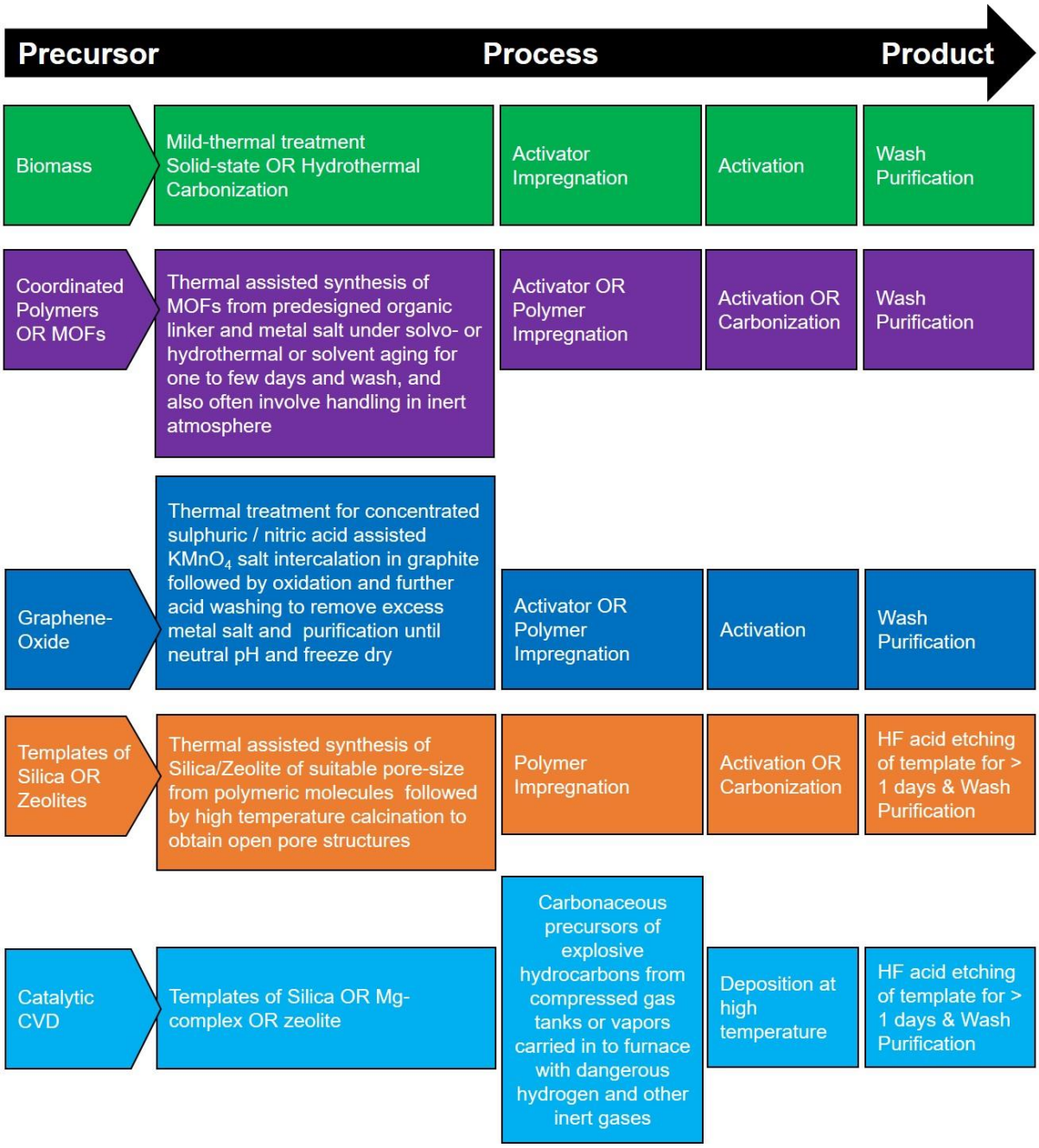

Figure S1. General synthesis steps (chemical manipulation and associated energetic steps) for the development of carbons from biomass and other structures involving coordinated polymers, MOFs, templates, vapours and graphene-oxide and by different methods.

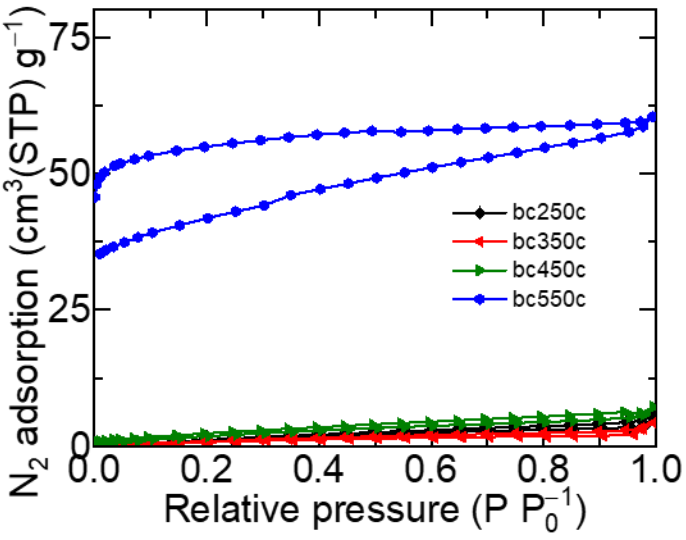

Figure S2. N_2 adsorption isotherms of biochars – accounts the negligible porosity with SSA_{BET} of (6-10) $m^2\ g^{-1}$ for BC250-450 samples and it is about 150 $m^2\ g^{-1}$ for BC550. The corresponding total pore volumes are ≈0.010 $cm^3\ g^{-1}$ and 0.093 $cm^3\ g^{-1}$, respectively.

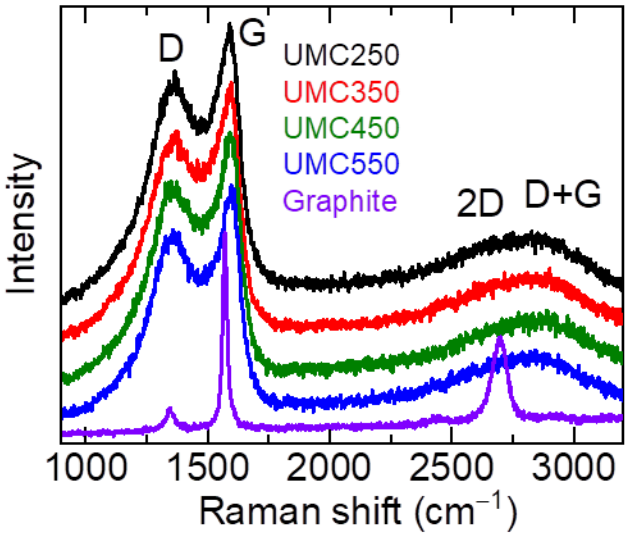

Figure S3. Raman spectra of UMCs; the graphite with corresponding D, G, 2D (overtone of the D band) and D+G bands near 1340 cm^{-1}, 1594 cm^{-1}, 2680 cm^{-1} and 2900 cm^{-1} respectively, are showed for comparative understanding. Clearly due to the porous nature the UMCs exhibit very different Raman features than graphitic structure.

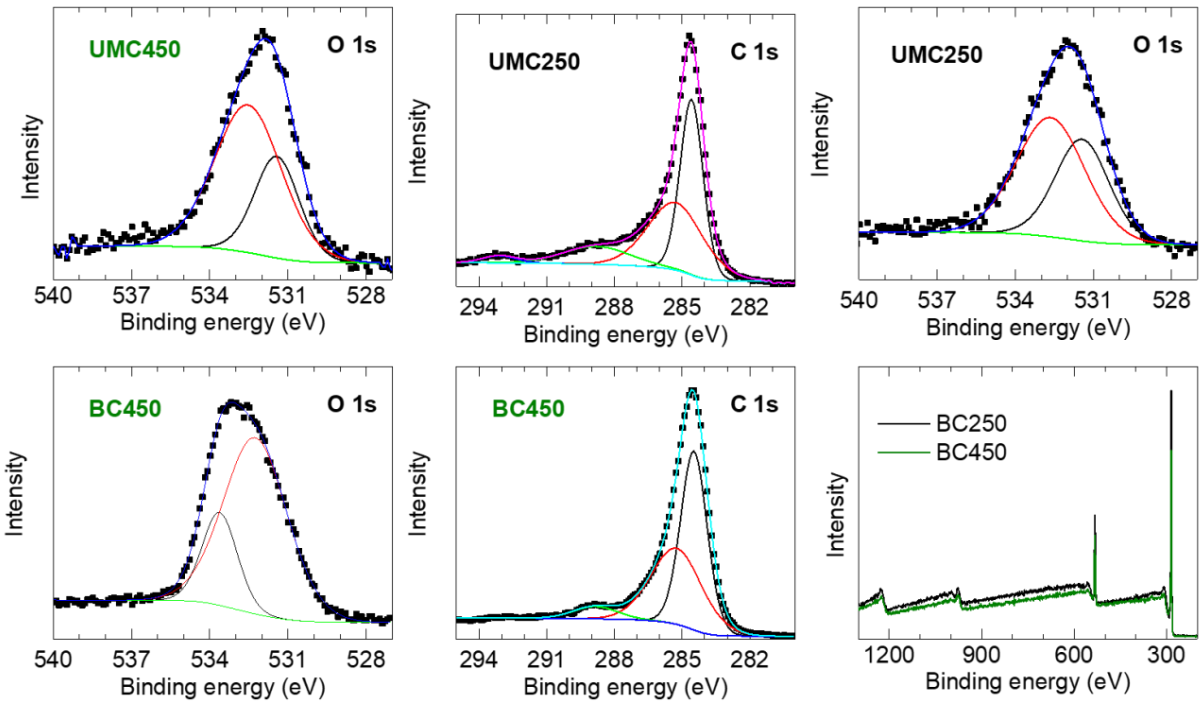

Figure S4. XPS spectra: Core level C 1s and O 1s, and survey are presented for UMC450, UMC250 and precursor BC450. Survey spectra indicate the C and O in the samples. Considerable changeover of the O 1s peak with respective variation of C–C and C=C components from BC450 to UMC450 indicates the development of microporosity in UMC450.

Table S4. Summary on the XPS elemental analysis.

Sample	C atom%	O atom%	Deconvolution of C 1s*			Deconvolution of O 1s	
			C=C (284.6 eV)	C–O (285.3 eV)	C=O (288.5 eV)	C=O (531.4 eV) (structure)	C–O (532.6 eV) (adsorbed)
UMC250	88.3	11.7	43.6%	40.2%	14.2%	37.6%	62.4%
UMC350	85.8	14.2	45.1%	33.7%	18.5%	31.1%	68.9%
UMC450	86.5	13.5	46.1%	37.1%	13.7%	31.3%	68.7%

* About 2-3% of O–C=O component is observed at 293.2 eV.

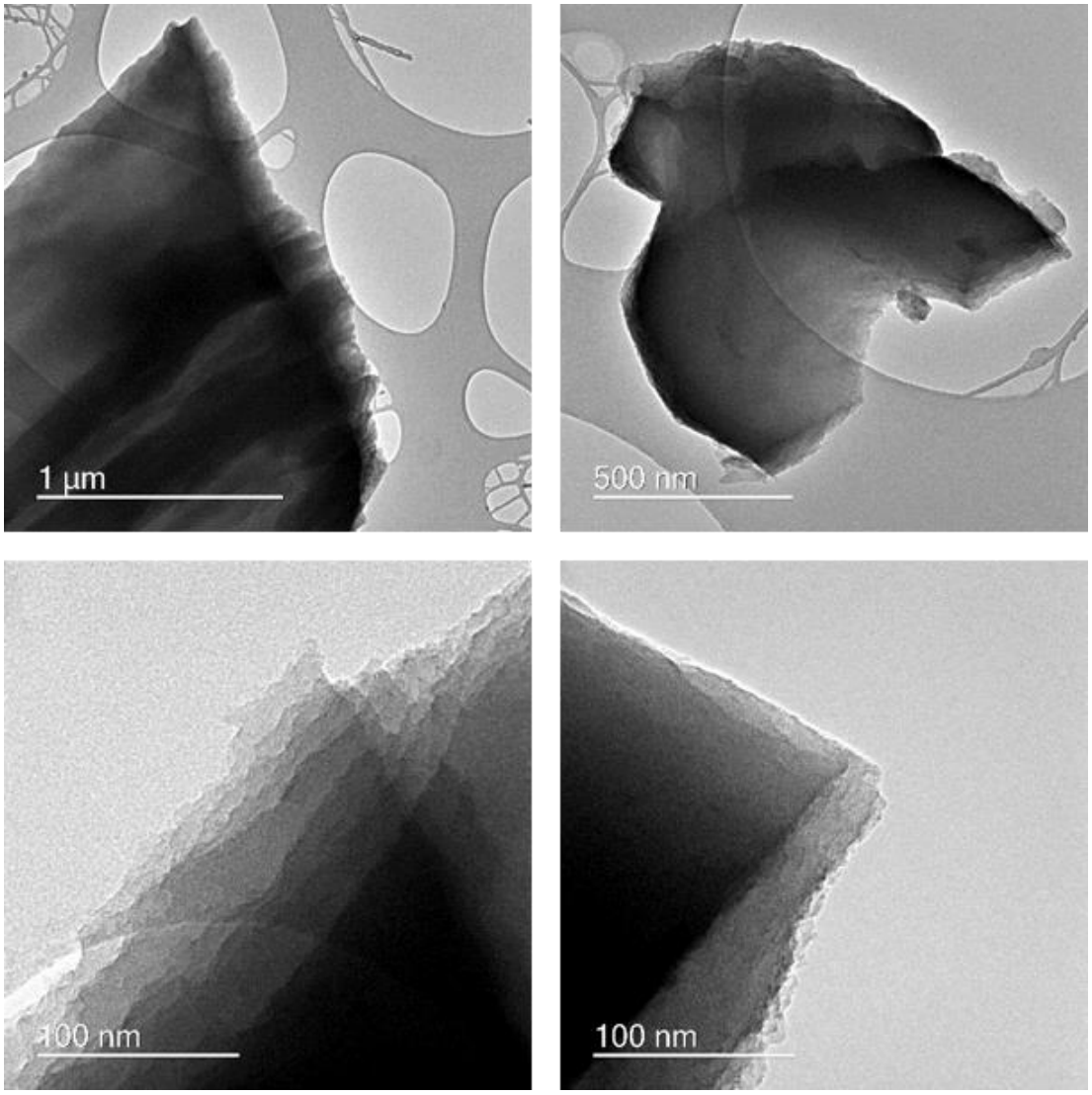

Figure S5. TEM micrographs of BC450.

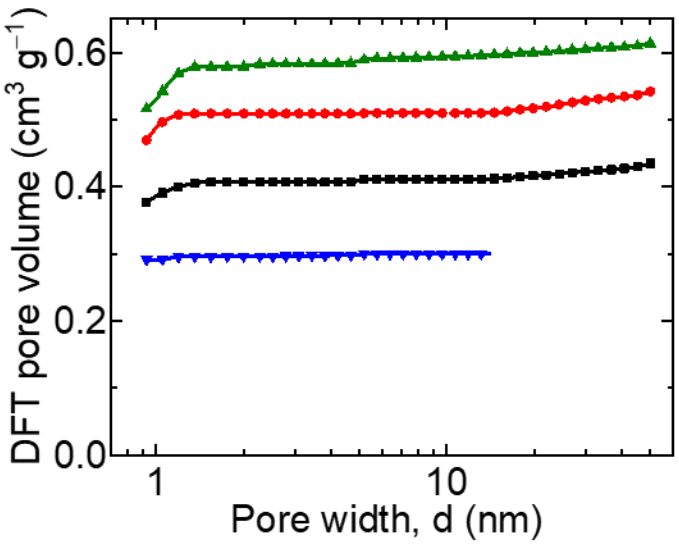

Figure S6. QSDFT derived pore-size distribution (left) and cumulative pore volume (right) curves with respect to the pore-width.

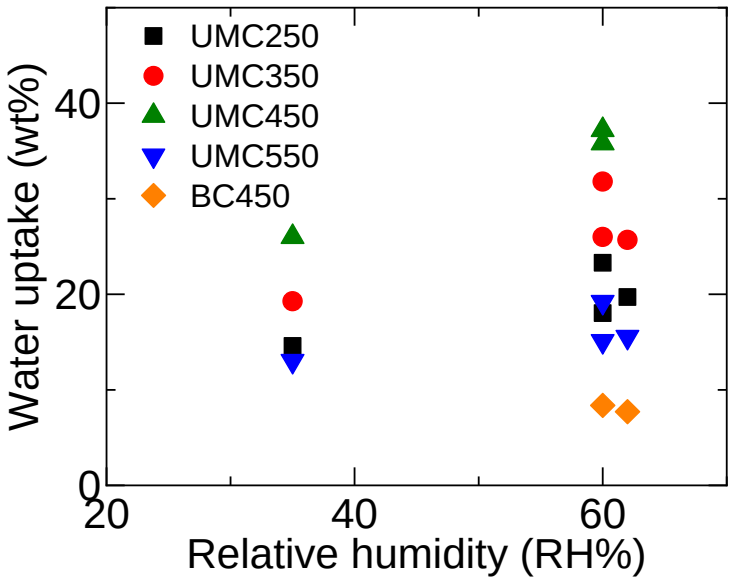

Figure S7. Water uptake capacity against relative humidity. The data is obtained with multiple adsorption-desorption tests.

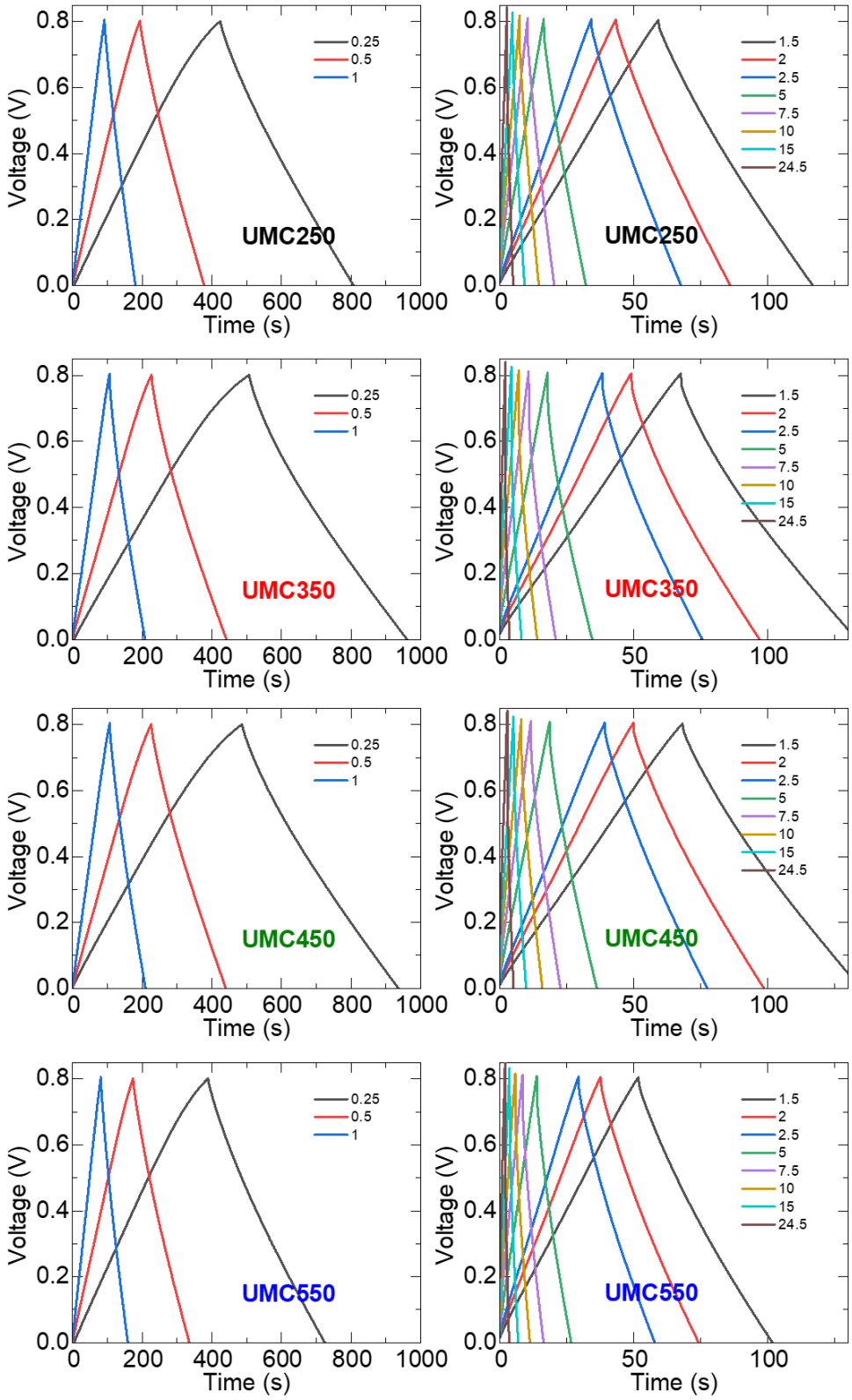

Figure S8. The GCD curves at different current densities between (0.25-24.5) A g^{-1} for all the samples: UMC250 (top row), UMC350 (second row from top), UMC450 (second row from bottom) and UMC550 (bottom row).

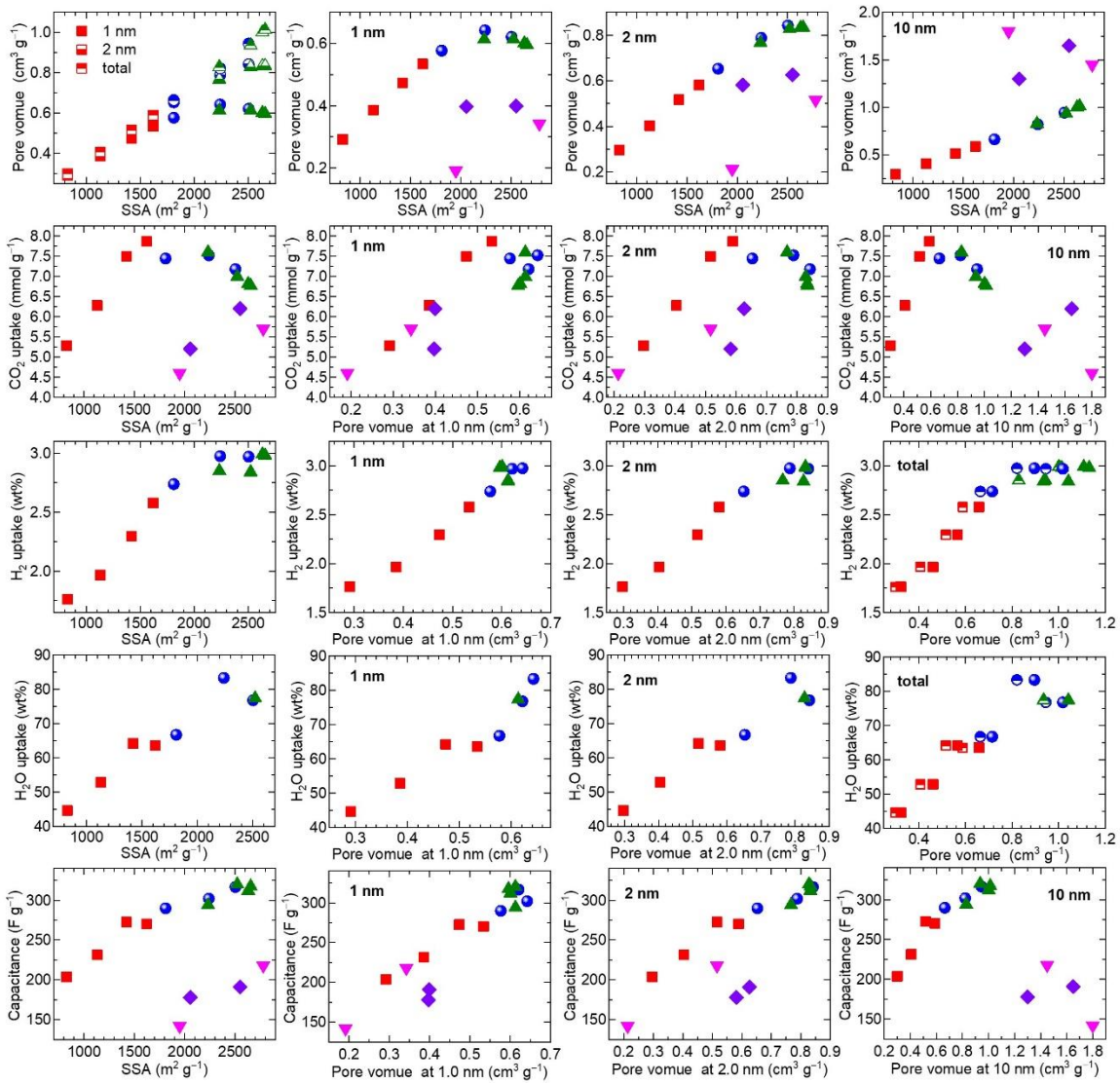

Figure S9. **Direct specific porosity dependence capacities for all case studies of CO_2, H_2, H_2O and EDLC: Top row:** Variation of DFT deduced pore volumes of specific pore-sizes against surface area. **The following rows second to bottom from top:** CO_2 , H_2, H_2O and EDLC capacities variation with respect to the SSA_{BET} (left panel), and pore volume at a specific pore widths, 1.0 nm (second left panel), 2.0 nm (third left panel) and 10.0 nm (right panel).

The CO_2 uptakes against SSA_{BET} is directly controlled with the corresponding porosity at ≤1.0 nm pore sizes. The capacities deviates from their linear trend when porosity is developed at increased pore widths. The increased pore size and its distribution at or above 1 nm size pores do not effectively contributing to the CO_2 uptakes. Thus the increased surface area in the NPCs with large pores show reduced capacity, which is also revealed by pore volumes associated with the large pores, at ≥1.0 nm pore sizes. Interestingly, the H_2, H_2O or EDLC (in aqueous electrolyte) capacities exhibit good correlation with the pore volume at 1.0 nm pore sizes.

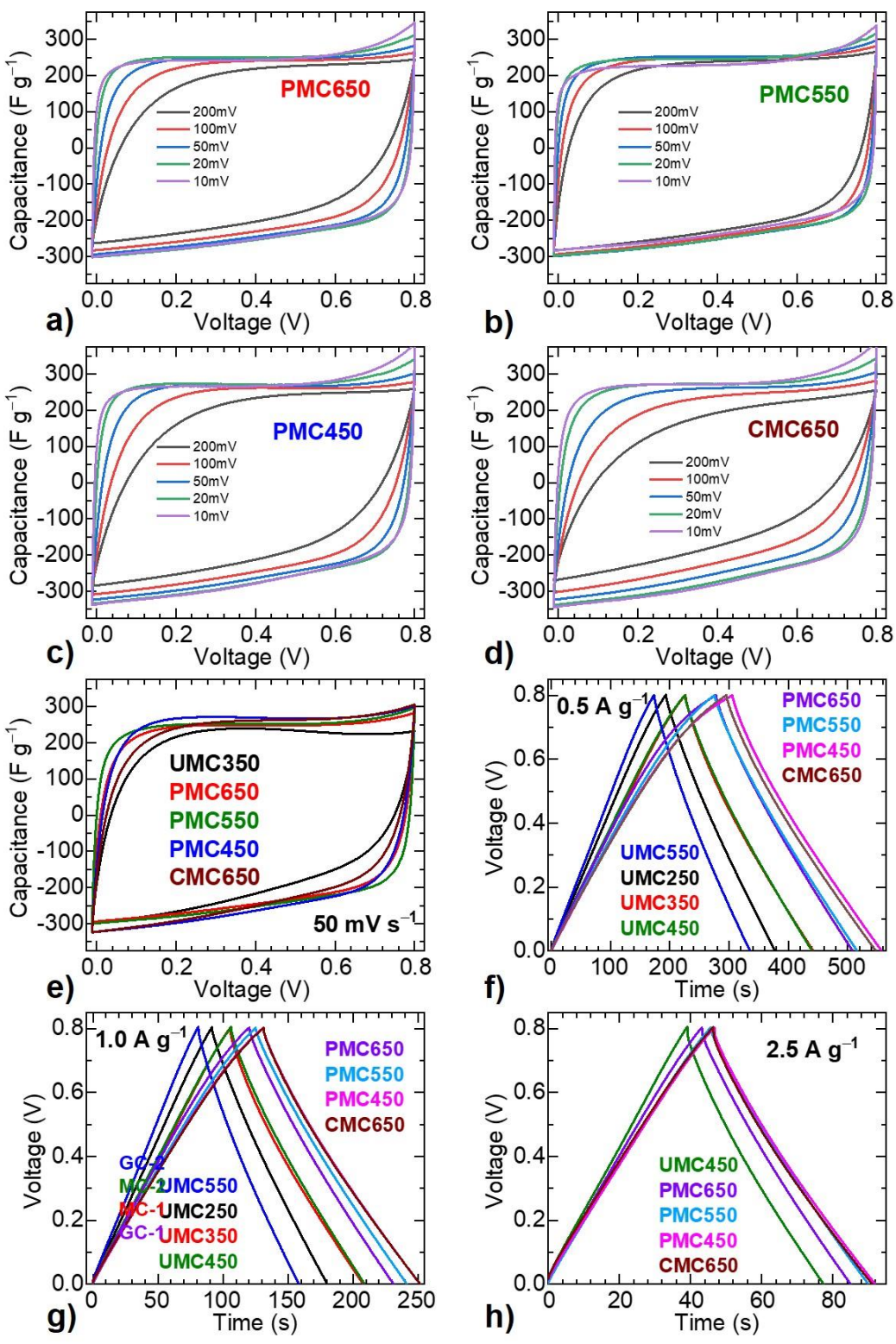

Figure S10. Supercapacitors in organic electrolyte: CV and GCD curves of UMCs, PMCs, and CMCs.